LAWRENCE
LIVERMORE
NATIONAL
LABORATORY

LLNL-JRNL-688670

Energy Measurements of K-shell Transitions in L-shell Ions of Si and S

N. Hell, G. V. Brown, J. Wilms, V. Grinberg, J. Clementson, D. Liedahl, F. S. Porter, R. L. Kelley, C. A. Kilbourne, P. Beiersdorfer

April 12, 2016

Astrophysical Journal

Disclaimer

Preprint typeset using LaTeX style AASTeX6 v. 1.0

LABORATORY MEASUREMENTS OF THE K-SHELL TRANSITION ENERGIES IN L-SHELL IONS OF SI AND S

N. Hell[1,2], G.V. Brown[2], J. Wilms[1], V. Grinberg[3], J. Clementson[2], D. Liedahl[2], F.S. Porter[4], R.L. Kelley[4], C.A. Kilbourne[4], P. Beiersdorfer[2]

[1]Dr. Karl Remeis-Sternwarte and Erlangen Centre for Astroparticle Physics, Universität Erlangen-Nürnberg, Sternwartstr. 7, 96049 Bamberg, Germany
[2]Lawrence Livermore National Laboratory, 7000 East Ave., Livermore, CA 94550, USA
[3]Massachusetts Institute of Technology, Kavli Institute for Astrophysics and Space Research, Cambridge, MA 02139, USA
[4]NASA-GSFC, 8800 Greenbelt Road, Greenbelt, MD 20771, USA

ABSTRACT

We have measured the energies of the strongest 1s–2ℓ (ℓ = s,p) transitions in He- through Ne-like silicon and sulfur ions to an accuracy of < 1 eV using Lawrence Livermore National Laboratory's electron beam ion traps, EBIT-I and SuperEBIT, and the NASA/GSFC EBIT Calorimeter Spectrometer (ECS). We identify and measure the energies of 18 and 21 X-ray features from silicon and sulfur, respectively. The results are compared to new Flexible Atomic Code calculations and to semi-relativistic Hartree Fock calculations by Palmeri et al. (2008). These results will be especially useful for wind diagnostics in high mass X-ray binaries, such as Vela X-1 and Cygnus X-1, where high-resolution spectral measurements using *Chandra*'s high energy transmission grating has made it possible to measure Doppler shifts of 100 km s^{-1}. The accuracy of our measurements is consistent with that needed to analyze *Chandra* observations, exceeding *Chandra*'s 100 km s^{-1} limit. Hence, the results presented here not only provide benchmarks for theory, but also accurate rest energies that can be used to determine the bulk motion of material in astrophysical sources. We show the usefulness of our results by applying them to redetermine Doppler shifts from *Chandra* observations of Vela X-1.

1. INTRODUCTION

Prominent absorption and emission X-ray features from highly charged silicon and sulfur ions have been detected and measured in a medley of celestial sources, including solar flares (Neupert 1971), other stellar coronae (e.g., Kastner et al. 2002; Huenemoerder et al. 2013), various types of Active Galactic Nuclei (e.g., Lee et al. 2001; Kaspi et al. 2002; Kinkhabwala et al. 2002; Holczer et al. 2007; Holczer & Behar 2012; Reeves et al. 2013), and high-mass X-ray binaries (HMXB; e.g., Sako et al. 2002; Boroson et al. 2003; Watanabe et al. 2006; Chang & Cui 2007; Hanke et al. 2008; Miškovičová et al. 2016). HMXBs, although well studied and cataloged, are not yet fully understood. In general, they consist of a massive O- or B-type star in orbit with a compact object, either a black hole or neutron star. X-ray emission or absorption features from these sources are generated when the luminous ($10^{36} \ldots 10^{38}$ erg s^{-1}) X-ray continuum from the accreting compact object irradiates, ionizes, and fluoresces the stellar wind material ejected from the companion star. Because the stellar wind of the massive companion is radiation driven, the ionizing nature of the X-ray continuum affects not only the wind structure, but also the mass loss rate of the companion star. Hence, Kα transitions originating in the wind have not only been used to determine the ion structure and motion of the wind, but also provide insight into the mass loss rate of the companion star and the strength of the X-ray continuum. For example, in the case of Vela X-1, Sako et al. (2002), Schulz et al. (2002), Goldstein et al. (2004), and Watanabe et al. (2006) report high resolution X-ray emission spectra from 2p→1s, i.e., Kα, transitions from both L- and K-shell silicon and sulfur ions. Sako et al. (2002) identify resolved line emission from O-like Si VII through H-like Si XIV, and an unresolved feature identified as Si II–Si VI. Goldstein et al. (2004) find the motion of different ions of the same element to be non-uniform, based on the limited quality of their used reference wavelengths. Watanabe et al. (2006) build a three dimensional Monte-Carlo radiative transfer model and report a mass loss rate for the companion star and the structure of the wind, although they do not analyze the line emission from the L-shell silicon ions, but only from H-like Si. In the case of Cygnus X-1, the Kα absorption features in L-and K-shell ions of silicon and sulfur have been measured and used to diagnose the nature of the stellar wind (Hanke et al. 2008; Hell et al. 2013; Miškovičová et al. 2016). Specifically, these features have been shown to be produced by "clumps" of onion-structured material, where the inner layers are colder, denser, and less ionized, moving in and out of the observational line of sight.

In the case of multielectron L-shell ions of silicon and sulfur, the utility of the associated X-ray line diagnostics is limited and often precluded by the relatively poor accuracy of the atomic reference data. Accurate calculations of the atomic structure of these ions is challenging because correlation effects among multiple electrons must be taken into account. Historically, Hartree-Fock calculations of House (1969) were used to interpret high resolution solar spectra (Fritz et al. 1967), and more recently have been used to analyze data from both Vela X-1 (Schulz et al. 2002; Goldstein et al. 2004) and Cygnus X-1 (Hanke 2011). However, House (1969) only provide simplified data listing only a single transition for each ion. To provide a more complete and accurate data set, more sophisticated calculations have been completed using more advanced atomic models. For example, Behar & Netzer (2002)

used the Hebrew University Lawrence Livermore Atomic Code (HULLAC; Klapisch 1971; Klapisch et al. 2006, and references therein) to calculate transition energies and line strengths for the strongest K-shell transitions in He- through F-like silicon and sulfur ions. At present, the most complete calculation is provided by Palmeri et al. (2008, P08), who use a semi-relativistic Hartree-Fock code to calculate level energies, transition wavelengths, and radiative decay rates for ∼1400 K-shell transitions in silicon and sulfur ions. The variation among the inner-shell transition energies calculated with various codes is ∼2–5 eV, i.e., on the order of several 100 km s^{-1} for the diagnostically important L-shell silicon Kα lines. This variation is comparable to the expected Doppler shift of the L-shell silicon Kα lines (Watanabe et al. 2006; Liedahl & Brown 2008; Miller et al. 2005, 2012; Miškovičová et al. 2016), and significantly larger than the systematic wavelength error of *Chandra*'s High Energy Transition Grating Spectrometer (HETGS), which is on the order of 100 km s^{-1} (Marshall et al. 2004; Canizares et al. 2005; Chandra X-ray Center 2015). Hence, the main systematic uncertainty in the determination of Doppler shifts from X-ray lines is our knowledge of atomic physics. This has been pointed out before in studies of the K-shell lines in L-shell oxygen ions (Schmidt et al. 2004; Gu et al. 2005).

When comparing atomic databases commonly used to interpret both Solar and extra-Solar X-ray spectra, the data from P08 are found in the Universal Atomic DataBase (uaDB) accompanying XSTAR (Bautista & Kallman 2001); however, they are not included in either the atomic physics for astrophysics database, AtomDB v2 (Foster et al. 2012) or the CHIANTI atomic physics database (Dere et al. 1997; Landi et al. 2013). AtomDB v2 only includes K-shell transitions in helium-like and hydrogen-like ions; CHIANTI only includes H-like, He-like, and Li-like transitions.

There is one previous measurement available for L-shell transitions in Be- through F-like Si and S ions. Faenov et al. (1994) measured transitions produced in a CO_2 laser-produced plasma. They also provided a comparison to their own theoretical calculations. The density of this plasma is significantly higher than typical densities in an astrophysical environment. The spectra reported by Faenov et al. (1994) therefore comprise mainly dielectronic satellites (see their Tables I and II) and are only of limited applicability for our purpose.

Here, we report results of measurements of the 1s–2ℓ (ℓ = s, p) K-shell energies in He- to Ne-like ions of silicon and sulfur in a coronal plasma produced with the Lawrence Livermore National Laboratory electron beam ion traps (Section 2). To gauge the systematic uncertainty inherent to calculations of many-body atomic systems, we compare these measurement results (Section 3.1) to line energy calculations performed with two popular atomic codes used for line identification, namely our own calculations with the Flexible Atomic Code (FAC; Gu 2004b, 2008) (Section 3.2) and the tables of P08 (Section 3.3). In addition, we list the centers of major line blends as a reference for observations with moderate resolution and derive new Doppler shifts for Vela X-1 based on our laboratory measured values (Section 4). We summarize our results in Section 5.

2. MEASUREMENT

2.1. *Experimental Setup*

The measurements presented here were carried out using the Lawrence Livermore National Laboratory (LLNL) electron beam ion traps, EBIT-I (Run-I) and SuperEBIT (Run-II). The details of their operation have been described elsewhere (Beiersdorfer 2008, 2003; Marrs et al. 1994; Levine et al. 1988; Marrs et al. 1988). In brief, highly charged ions are produced, trapped, and excited by EBIT using a near monoenergetic electron beam and an electrostatic trap. Several methods have been developed to inject elements for study (Brown et al. 1986; Schneider et al. 1989; Elliott & Marrs 1995; Ullrich et al. 1998; Niles et al. 2006; Yamada et al. 2007; Magee et al. 2014). For the experiments described here, neutral sulfur and silicon were injected into the EBIT's trap region as gaseous SF_6 and $C_{10}H_{30}O_3Si_4$, respectively, using a well collimated ballistic gas injector. Once the neutral material intersects the electron beam, the molecules are broken apart and resulting atoms are collisionally ionized and trapped. To avoid the build up of high-Z material, such as tungsten and barium originating from the electron gun, the trap region is emptied and refilled periodically, on a time scale of tens of milliseconds.

The electron impact excitation energies of the K-shell transitions in the silicon and sulfur ions are $\gtrsim$1.73 keV, while the ionization energies for the L-shell ions range from 166.8 eV for Ne-like Si v to 707.2 eV for Li-like S xiv (Cowan 1981). Hence, in order to excite the Kα lines the electron beam energy must be ∼ 3–10 times the ionization threshold. Under typical operating conditions at these energies, the charge state distribution would be dominated by lithium- and helium-like ions. In order to produce a significant amount of lower charge states at the high electron impact energies required for inner-shell excitation, several methods have been developed (Decaux & Beiersdorfer 1993; Schmidt et al. 2004). In the present experiment, the neutral gas injection pressure is set to values several orders of magnitudes larger than EBIT's base pressure of $\lesssim 10^{-10}$ Torr, short refill cycle times and relatively low electron beam currents were employed. Together, these operating parameters yield a significant fraction of low charge states at high electron impact energy. The spectral signature of significant amounts of several L-shell ions can easily be seen in the X-ray spectra (see Figure 1). Note that the electron beam energies employed at these measurements were well away from any dielectronic recombination resonances of the respective measured elements, i.e., the emission lines originate entirely from electron impact excitation and inner-shell ionization, contrary to the laser experiments reported by Faenov et al. (1994).

The spectrum of the X-ray radiation from the trapped ions is recorded with the 16 low-energy pixels of the EBIT Calorimeter Spectrometer (ECS; Porter et al. 2008a,b, 2009a,b), designed and built by the NASA/GSFC Calorimeter group. The ECS is the improved successor of the XRS/EBIT (Porter et al. 2004, 2008c), the engineering model of the *Astro-E2*/*Suzaku* calorimeter. The energy resolution of the ECS for these measurements was 4.5–5.0 eV, typical for the ECS. The spectra shown here are similar in quality to a spectrum measured

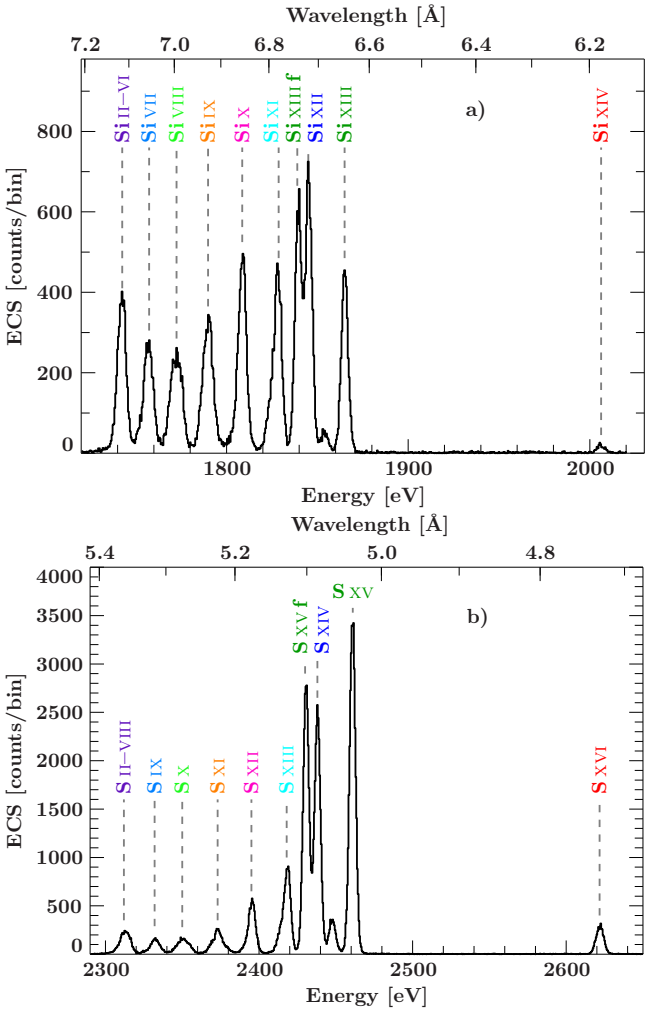

Figure 1. Calibrated and summed *a)* silicon and *b)* sulfur spectra from all 16 low-energy ECS pixels (Run-I). The color code of the ion labels is used whenever we specifically distinguish between isoelectronic sequences throughout this work.

with the Soft X-ray Spectrometer (SXS) system (Mitsuda et al. 2010) aboard the *Astro-H*/*Hitomi* X-ray observatory (Takahashi et al. 2010) or in the planned X-IFU instrument on *Athena* (Nandra et al. 2014; Ravera et al. 2014).

To assess the systematic errors in our measurement, we conducted a second experimental run using SuperEBIT (Run-II). SuperEBIT is the high-energy variant of EBIT-I used in Run-I and can achieve electron beam energies up to 250 keV (Beiersdorfer et al. 2003). SuperEBIT was used for Run-II because of beam time availability.

2.2. *Calibration*

Because of slight variations in performance, each pixel in the ECS array is calibrated separately. The energy scale for each pixel is determined by fitting 4th order polynomial functions to the measured pulse heights in volts space of known reference emission lines (Porter et al. 1997; Cottam et al. 2005); here, the X-ray line emission from K-shell transitions in He-like ions (Kα / line w: $1s\,2p\,{}^1P_1 \rightarrow 1s^2\,{}^1S_0$; K$\beta$: $1s\,3p \rightarrow 1s^2$; Kγ: $1s\,4p \rightarrow 1s^2$) and H-like ions (Ly α: $2p \rightarrow 1s$; Ly β: $3p \rightarrow 1s$). Specifically, for the Run-I measurement, the 1.7 to 1.9 keV band containing the lower charge states of silicon was calibrated with Kα, Ly α, Kβ, and Ly β lines of neon and silicon. For the 2.3 to 2.5 keV band containing the lower charge states of sulfur, Kα, Ly α, and Kβ of sulfur and Kα–Kγ of fluorine were used. For Run-II, Ne and S Kα, Ly α, and Kβ, and Si Kα–Kγ and Ly α were used to calibrate the silicon spectra, and Ne Kα, Ly α, and Kβ, Si and S Kα and Ly α, and Ar Kα were used to calibrate the sulfur spectra.

The reference wavelengths of the He-like systems used for calibration originate from Drake (1988) in case of the $1s\,2p \rightarrow 1s^2$ resonance line labelled "w" in the notation of Gabriel (1972). The wavelengths for $1s\,3p \rightarrow 1s^2$ Kβ and $1s\,4p \rightarrow 1s^2$ Kγ Rydberg states were taken from Vainshtein & Safronova (1985) and corrected for the ground state of Drake (1988) according to Beiersdorfer et al. (1989). Values for the Lyman series in the H-like systems are from Garcia & Mack (1965). The wavelengths were converted to energy using $E = hc\lambda^{-1}$ where hc = 12398.42 eV Å (with values for h, c and e from CODATA 2014, Mohr et al. 2015).

2.3. *Quality of the Calibration*

After calibration, the ECS events were binned to an energy grid of 0.5 eV. Figure 1 shows the summed Si and S spectra of all 16 low-energy ECS pixels for Run-I. To gauge the accuracy of the energy scale, the location of the H-like Ly α lines and the He-like line w of Si and S are determined from a simultaneous fit of the calibrated Run-I and Run-II spectra. The fitted values are then compared to the initial reference values. Table 1 shows the value from the comparison as well as from our FAC calculation, which is used as a guide for line identification (see below, Section 3.2). For silicon line w, the calibrated values are 0.16 eV lower than the reference values, for sulfur line w, they are 0.017 eV lower. For the S Ly α lines, the difference between theory and experiment is slightly larger, but still well below 0.5 eV (Table 1). Combining the uncertainties of the Ly α and w lines amounts to 0.13 eV for silicon and 0.23 eV for sulfur, which are taken as the systematic uncertainties. FAC results agree with Drake (1988) to within 0.2 eV in case of the transition energies in He-like ions, and within 0.03 eV for the transition energies in H-like ions.

The fitted widths of the He-like lines of about 4.5–5.0 eV are consistent with the expected energy resolution of the ECS in this energy region.

Table 1. Calibration results

Z	line	FWHM (eV)	line energy (eV)			$\Delta E_{\rm ref}$	$\Delta E_{\rm FAC}$
			fit	reference	FAC		
Si	w	$4.36^{+0.08}_{-0.12}$/4.92 ± 0.12	1864.84 ± 0.05	1864.9995	1864.812	−0.16	0.03
Si	Ly α	—	$2005.59^{+0.17}_{-0.20}$	2005.494[a]	2005.516[a]	0.10	0.07
S	w	4.55 ± 0.04/4.98 ± 0.14	2460.609 ± 0.018	2460.6255	2460.417	−0.017	0.191
S	Ly α_1	—	$2622.97^{+0.18}_{-0.26}$	2622.700	2622.730	0.27	0.24
S	Ly α_2	—	$2620.00^{+0.21}_{-0.34}$	2619.701	2619.731	0.30	0.27

[a] Mean value of Ly α_1 and Ly α_2 weighted by their statistical weights.

NOTE—Comparison between the fitted line centers (fit) of the He-like $1s\,2p \rightarrow 1s^2$ line w with the reference value (reference) of Drake (1988) and of the H-like $2p \rightarrow 1s$ Ly α lines of Si and S with the values of Garcia & Mack (1965), which were used for calibration. The full width half maximum (FWHM) determined from line w (used as detector resolution throughout the fits) is listed for Run-I / Run-II. ΔE_i gives the difference between the fit and the respective theoretical values. Listed uncertainties are purely statistical.

3. SPECTRAL ANALYSIS

3.1. *Fit Method*

In order to determine the transition energies of as many individual lines as the data allow, the spectra from Run-I and Run-II were fitted simultaneously for each element, using the Interactive Spectral Interpretation System ISIS (Houck & Denicola 2000; Houck 2002; Noble & Nowak 2008). The modeled energy range spans 1720–1880 eV for the Si spectra and 2290–2480 eV for the S spectra. The models for Run-I and Run-II consist of a sum of individual Gaussian lines, where the centers of these lines are tied between Run-I and Run-II, their widths are fixed to the respective resolution (Table 1), and their normalizations are left to vary freely. Fixing the line widths is valid because the natural line widths and the Doppler widths are small compared to the resolution of the calorimeter, no other line broadening mechanism is present in these experiments, and the energy resolution of the calorimeter is constant over these small energy ranges. In order to account for the flux above background found between the main peaks of the spectra, e.g., Figure 2, the models include a single second order polynomial for each dataset. A possible explanation for the presence of this continuum are weak unresolved lines (see Figure 5 in Section 3.3), low-energy spectral redistribution due to photon and electron escape events (Cottam et al. 2005), or some combination of both.

In order to determine the number of Gaussian components required to describe the data, we test the statistical significance of each line. A Monte Carlo type simulation (see `mc_sig` of the Remeis ISISscripts), generates 10^3 realizations of fake spectra based on the existing best fit model: for each energy bin of the fake spectrum, it draws a random number from a Poisson distribution with the mean equal to the modeled value. These fake spectra are fitted with the model used to create them (model A) and with a model containing an additional Gaussian line (model B). Because of the increased number of degrees of freedom, the χ^2 value for model B will be at least slightly better than the χ^2 for model A. The additional line

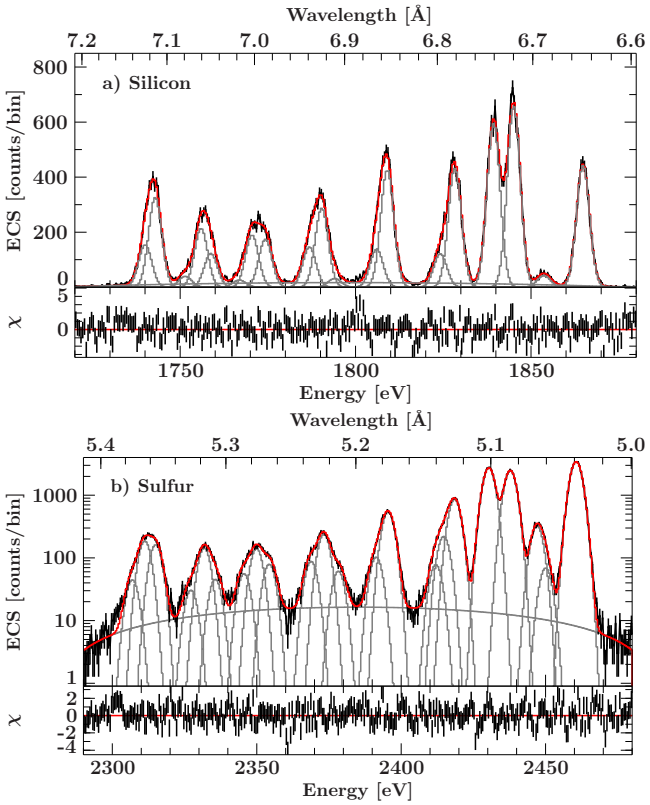

Figure 2. Overview over the components fitted to the Si (top) and S (bottom) spectra. The data are shown in black, the red line shows the total model, model components are gray.

in model B is only accepted if the improvements, $\Delta\chi^2_{{\rm fake},i} = \chi^2_{{\rm B},i} - \chi^2_{{\rm A},i}$, of 99% of the simulated cases are smaller than the improvement in the real spectrum. Figure 2 shows the final distribution of the single Gaussian components for silicon and for sulfur. Tables A1 and A2 list the resulting line centers with their statistical 90% confidence limits.

As an additional consistency check for the accuracy of our results, in a second approach we allow for a constant shift

of the Run-II data compared to the Run-I data. The derived constants of $0.13^{+0.06}_{-0.05}$ eV for Si and -0.12 ± 0.05 eV for S are consistent with our estimate of the systematic uncertainty of our calibration (Section 2.3).

3.2. *Line Identification with FAC*

To identify the lines associated with our measured spectra, we use FAC (Gu 2004b, 2008) to calculate the wavelengths of transitions in the involved ions and model the measured spectra. FAC is a compound package based on a fully relativistic ansatz via the Dirac equation which provides functions to calculate the atomic structure, bound-bound and bound-free processes, and includes a collisional ionization equilibrium code to estimate the line intensities for given plasma conditions (electron beam properties or plasma temperatures; Gu 2004a). The accuracy of FAC, determined from comparisons between FAC and experiments, is a few eV or 10–30 mÅ at ~10Å for energy levels (other than H-like) and 10–20 % for radiative transition rates and cross sections (Gu 2004a).

Our FAC calculations take into account radiative (de-)excitation, collisional (de-)excitation and ionization, autoionization, dielectronic recombination, and radiative recombination. At EBIT densities, the coronal limit applies, i.e., electron impact collisional excitation, inner-shell ionization, and subsequent radiative cascades are the main processes to populate upper states. At the electron beam energies used here, no emission from dielectronic recombination exists for the ions of interest and no X-rays from radiative recombination fall into our energy band. Although the main application for our results is photoionized plasmas, the collisional nature of EBIT does not compromise this task.

Our calculations include emission from all the $n \rightarrow 1$ transitions in Na-like to H-like silicon and sulfur, where $2 \leq n \leq 5$, allowing interactions between all levels, including $\Delta n = 0$ transitions. For these limits, the calculation could be completed in a reasonable time. The contribution to the line strength from higher n transitions is negligible. Since the charge state distribution in EBIT depends on ionization and recombination processes, the level populations are estimated for all ions in a single calculation. The other plasma code parameters are the electron beam energy, which we assume to follow a Gaussian distribution with an energy spread of $\sim$ 40 eV (Beiersdorfer et al. 1992; Gu et al. 1999), and an electron density of 10^{12} cm^{-3}, which we estimate from beam current and energy. The relative abundances of the trapped ions are set to be 1. The simulation of the spectrum produced in the trap is therefore not self-consistent.

Figure 3 illustrates the resulting FAC simulations for silicon and sulfur, considering the presence of H- through Na-like ions. The line centers of transitions calculated by FAC are convolved with a Gaussian line with a FWHM of 4.6 eV, i.e., the resolution of the calorimeter (see Section 2.3).

While the strongest K-shell line features from each charge state are easily resolved (Figures 1 and 3), identifying the transitions that contribute to each feature is accomplished by comparison to the FAC calculation as follows. For each feature we plot the data and individual model components and overlay them with the transitions obtained from FAC (Figures A1 and A2). Then we assume that for every Gaussian fit component the main contribution comes from the strongest FAC lines at this energy and identify the model component with these lines. The results are listed in Tables A1 (Si) and A2 (S). In each row the FAC lines are followed by the corresponding transitions as calculated by P08 (see Section 3.3 for details) and CHIANTI, if available. For most measured peaks, the distribution of the FAC lines agrees well enough with the measurements to allow a reliable identification. Both the Si and S spectra behave very similarly, so our description of the spectra here focuses on the contributions by iso-electronic sequence, for the most part not distinguishing in Z except in the rare cases where significant differences occur between the Si and S spectra.

The main Li-like, Be-like, and B-like features are each dominated by a single strong transition that is easily reproduced by the Gaussian components fitted to the spectra (see features labeled Li-2, Be-1, B-1 in Figures A1 and A2 panels

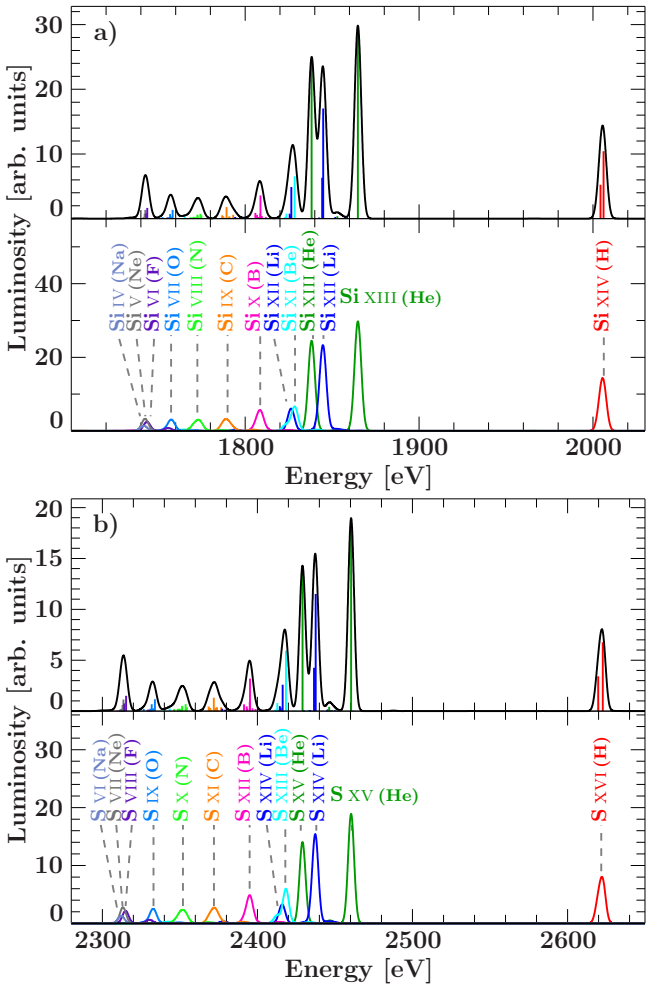

Figure 3. FAC simulation of the *a)* Si and *b)* S Kα spectra. For each subfigure the top panel shows the transition energies with their predicted luminosity and the total spectrum (black line) resulting from a convolution with Gaussians at the resolution of the ECS. The bottom panels show the convoluted spectra individually for each ionization state, which sum to the black line of the top panel. The impact of line blends can be seen quite clearly. Labels include the corresponding iso-electronic sequence in parentheses.

e-g). Although there are a few weaker transitions surrounding these strong lines, they do not strongly affect the fitted line centers. Both the Be- and B-like features have a low-energy shoulder caused by weaker transitions that have a just large enough separation from the strong transition to be resolved. According to our FAC calculations, the Li-like ion also has a relatively strong transition that sits right between the Be-like lines. Although in the synthetic Si spectrum the Li-like line appears to have similar strength as the strong Be-like line, a comparison of Figure 3 to the measured Si spectrum shows that due to the incorrect assumption of charge balance entering our simulation, the synthetic spectra overestimate the Li-like features relative to the Be-like ones. Accordingly, despite this Li-like transition being unresolved in Si, it does not seem to affect the fitted line centers of the Be-like transitions Be-1 and Be-2 much (Figure A1, panel f). For S on the other hand (Figure A2, panel f), the Li-like transitions are attributed to their own Gaussian component (Be-2) while the weak Be-like line is assigned to a separate component (Be-3).

The transition rich spectra of the lower charge states C-like, O-like, and N-like are more complex as they have many transitions of similar strength rather than a distinct strong transition among a few weak ones (Figures A1 and A2, panels b-d). However, some of these transitions tend to cluster into groups. The separation of these groups is larger for the higher-Z element S, making it easier to partially resolve them. As discussed for iron by Decaux et al. (1997), starting around C-like ions the Kα line emission of the lower charge states probably has strong contributions from states excited through inner-shell ionization in addition to the collisionally excited states.

In the C-like ions (Figures A1 and A2, panel d), the strongest fitted component, C-2, is made up of the strongest calculated transitions at slightly lower energies than the component's center and a few weaker transitions at and slightly above the fitted energy. The C-like feature also has a strong low-energy shoulder (C-3) from transitions similar in strength to the ones from the C-2 cluster, and a weaker high-energy shoulder (C-1) consisting of a C-like and two weak Li-like transitions.

The N-like transitions split into four main groups (Figures A1 and A2, panel c). They are accompanied by a Be-like transition in the low-energy tail of their spectral feature. Again, the larger spacing in S is beneficial, although in both Si and S this feature is modeled by three components. While N-1 coincides well with the first group of calculated transitions on the high-energy side for both components, the second group containing the other two of the strongest four transitions falls right between N-1 and N-2 in Si, but is clearly attributed to N-2 in S. N-2 also encompasses the third group of transitions, while N-3 contains the last group of N-like transitions and the mentioned Be-like transition.

The O-like peak is also described by three Gaussians (Figures A1 and A2, panel b). The strongest line calculated with FAC makes up the weaker component at high energies (O-1), while the main component (O-2) consists of a number of weaker transitions. A single O-like transition accounts for the low-energy shoulder (O-3).

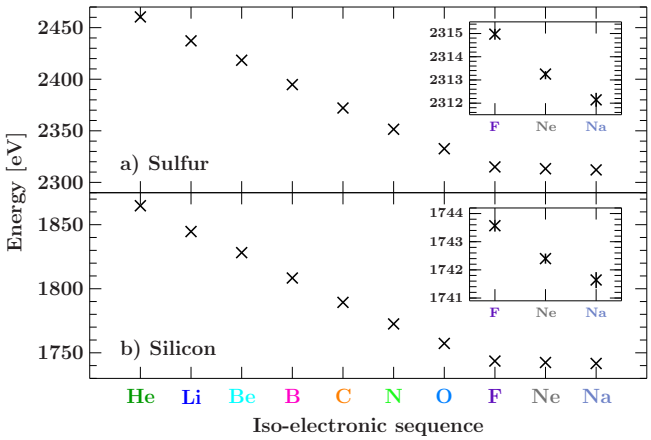

Figure 4. Energies of the line centers for different ionization stages of sulfur (a) and silicon (b), derived from FAC calculations. Lines for ions with more than 9 electrons (F-like) blend strongly with a predicted energy spacing of ~ 1 eV between charge states.

The lowest energy peak (Figures A1 and A2, panel a) consists of a blend of K-shell transitions in F-like ions as well as emission from lower charge states (Figure 4). This is a result of the fact that, for charge states other than F-like, emission is dominated by innershell ionization followed by radiative decay in these cases and the effect of additional spectator electrons in $n \geq 3$ shell on these transition energies is relatively small. Additionally, owing to the open $n = 3$ shell, the M-shell ions have a more complex energy level structure – and, therefore, a multidue of transitions – in each of these charge states. The energy ranges covered by these transitions overlap severely (Figure 5). Specifically, the Kα transition energies from these charge states fall within a 3 eV energy band and are therefore unresolved (Figure 4). Consequently, although the F-like ion only has two distinct transitions, we cannot resolve this charge state individually from the transitions in M-shell ions in these low-Z elements. This last peak is modeled by two (Si) and three (S) Gaussian components, respectively. In both cases, we attribute the first, i.e., high-energy component (F-1) to a mixture of transissions in F-like and Ne-like ions. In case of the Si X-1 line at 1740.04 eV, however, there are no lines of considerable strength in our calculations that could be used for identification. We tentatively identify this line as a blend of Kα emission from very low charge states with more than 10 electrons. Similarly, although Table A2 lists weak transitions in Na-like S VI and B-like S XII for the lines F-2 and F-3, these lines probably also have a significant contribution from weak lines from near-neutral ions, as discussed for the case of silicon.

Also notable is that for both Si and S, line z as calculated with FAC (Si: 1838.20 eV, S: 2429.075 eV) has a large offset (>1 eV) compared to the measured line center (Si: 1839.33 eV, S: 2430.380 eV). Our measurement is, however, consistent with the reference values reported by Drake (1988, Si: 1839.448 eV; S: 2430.347 eV).

3.3. *Comparison with Palmeri et al. (2008)*

For completeness and to provide a test for the accuracy of the Kα line energies employed by XSTAR, we compare our measurements and our FAC calculations to those of P08. Note

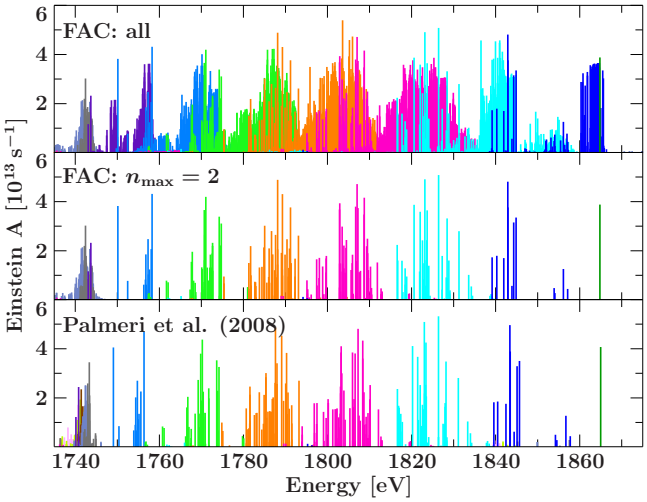

Figure 5. Comparison between the atomic data of Si presented by P08 (*bottom*) and the calculation with FAC (*middle*: only $2\ell \rightarrow 1s$ transitions as in P08; *top*: all calculated transitions in this shown energy range, including satellites with an electron in up to the $n_{max} = 5$ shell) for He- through Ne-like ions. Different colors represent different ionization states (see Figure 1).

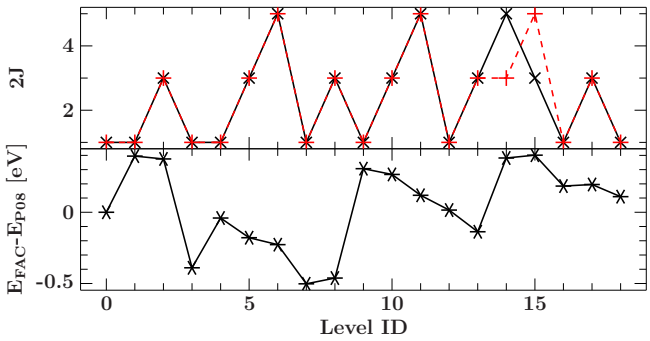

Figure 6. Comparison between FAC and P08 energy levels for Li-like Si. The top panel shows two times the total angular momentum (black: FAC, red: P08) of the levels sorted by energy, where the level ID equal to zero corresponds to the ground state (see Table 2). The lower panel displays the difference between these energies of the two calculations.

that the calculated transition wavelengths listed by P08 have been empirically shifted by P08 for ions with $3 \leq N \leq 9$, where N is the number of electrons. A qualitative comparison between the results obtained with FAC and the lines published by P08 is displayed in Figure 5 for silicon. Since the P08 data do not provide luminosities, the line distributions are shown via their radiative transition rates (Einstein A). P08 only list $2\ell \rightarrow 1s$ transitions. We therefore also filter for these lines calculated with FAC. The transitions with a spectator electron in a higher n shell blend strongly with Kα transitions of the next ionization state, but according to the FAC calculations, their contribution to the Kα line strength is negligible (Figure 3).

As expected, the positions of the He-like lines agree very well. For lower ionization states, the general distribution of the lines is still similar, but the predicted energy separation of some line features does not agree. For example, there are two O-like Si VII lines around 1750 eV (Figure 5), specifically the transitions $1s^2 2s 2p^5\ {}^1P^o_1$ – $1s 2s 2p^6\ {}^1S_0$ and $1s^2 2s^2 2p^4\ {}^1S_0$ – $1s 2s^2 2p^5\ {}^1P^o_1$ (P08) respectively $(1s^2\ 2s_{1/2}\ 2p^2_{1/2}\ (2p^3_{3/2})_{3/2})_1$ – $(1s_{1/2}\ 2s_{1/2}\ 2p^2_{1/2}\ 2p^4_{3/2})_0$ and $1s^2\ 2s^2\ 2p^2_{1/2}\ (2p^2_{3/2})_0$ – $(1s_{1/2}\ 2s^2\ 2p^2_{1/2}\ (2p^3_{3/2})_{3/2})_1$ (FAC), for which the ratio of the transition probabilities is approximately the same in both calculations (P08: 0.21; FAC: 0.20). The separation of their line energies, however, is almost twice as large in FAC (2.32 eV) as in P08 (1.33 eV). The most outstanding difference is that in the P08 calculations the two F-like spectral lines at ~ 1741 eV have distinctly lower energies than the Ne-like lines, although the Ne-like iso-electronic sequence has an electron more than the F-like ions. This behavior is in contrast to the FAC calculations where the F-like lines have higher energies.

Comparing FAC (jj-coupling) and P08 (LS-coupling) is not trivial since the two calculations are based on different coupling schemes. It is therefore necessary to translate one scheme into the other. The calculations are in sufficient agreement such that most lines can be identified through a comparison of the line lists instead of resorting to a complicated formal mapping between both schemes (see, e.g., Calvert & Tuttle 1979; Dyall 1986). We do this comparison by first sorting the levels of both calculations according to energy and then matching the levels in order of increasing energy. The match is cross-checked via the total angular momentum J, which is the only good quantum number common between the two coupling schemes and therefore should be identical between them. In cases where J does not match between two assigned levels, LS-coupling multiplets can be rearranged for their Js to fit the jj-coupling partners. This is possible because within these multiplets the differences between the calculated level energies are smaller than the estimated uncertainty of the calculations and, in most cases, smaller than the energy differences between P08 and FAC results.

As an example, Table 2 lists the sorted energy levels of Li-like Si XII for both FAC and P08. Figure 6 shows a comparison of their total angular momenta. The energy differences between the levels from different calculations are within their stated accuracy of at least 2 eV. The levels with IDs 14 and 15 are mismatched in their J. These levels belong to the doublet ^{2}D, with a fine structure splitting of roughly 0.1 eV. This difference is small compared to the ~0.4 eV between FAC and P08. For practical purposes we therefore assume that FAC level 14 corresponds to P08 level 15 and vice versa. The results are listed in Tables A1 and A2.

4. CENTER OF LINE BLENDS

In most experimental cases, the spectral resolution is not adequate to distinguish between single features of the given lines. This is especially true for satellite based instrumentation. Therefore, the ability to determine the energy for each identified line is precluded. In order to provide the means to derive Doppler shifts also for these cases, in a second approach we fit the spectra with a single Gaussian for each of the readily distinguishable line blends, leaving the line widths free to vary. The obtained line centers, which are listed in Table 3 and displayed in Figure 7, are sufficient as reference energies to derive Doppler shifts for collision dominated or photoionized plasmas where 1s–2p transitions are dominant,

Table 2. Comparison of the FAC and P08 energy levels of Li-like Si.

Level	FAC / *jj*-coupling			P08 / *LS*-coupling		
ID	label	$2J$	E (eV)	label	$2J$	E (eV)
0	$1s^2\,2s_{1/2}$	1	0.0000	$1s^2 2s\ ^2S_{1/2}$	1	0.0000
1	$1s^2\,2p_{1/2}$	1	24.2019	$1s^2 2p\ ^2P^o_{1/2}$	1	23.8072
2	$1s^2\,2p_{3/2}$	3	25.1920	$1s^2 2p\ ^2P^o_{3/2}$	3	24.8172
3	$1s_{1/2}\,2s^2$	1	1819.3742	$1s2s^2\ ^2S_{1/2}$	1	1819.7636
4	$((1s_{1/2}\,2s_{1/2})_1\,2p_{1/2})_{1/2}$	1	1825.5977	$1s(^2S)\,2s2p(^3P^o)\ ^4P^o_{1/2}$	1	1825.6379
5	$((1s_{1/2}\,2s_{1/2})_1\,2p_{1/2})_{3/2}$	3	1825.8735	$1s(^2S)\,2s2p(^3P^o)\ ^4P^o_{3/2}$	3	1826.0523
6	$((1s_{1/2}\,2s_{1/2})_1\,2p_{3/2})_{5/2}$	5	1826.5509	$1s(^2S)\,2s2p(^3P^o)\ ^4P^o_{5/2}$	5	1826.7783
7	$((1s_{1/2}\,2s_{1/2})_0\,2p_{1/2})_{1/2}$	1	1844.2892	$1s(^2S)\,2s2p(^3P^o)\ ^2P^o_{1/2}$	1	1844.7912
8	$((1s_{1/2}\,2s_{1/2})_0\,2p_{3/2})_{3/2}$	3	1844.8632	$1s(^2S)\,2s2p(^3P^o)\ ^2P^o_{3/2}$	3	1845.3252
9	$(1s_{1/2}\,(2p^2_{1/2})_0)_{1/2}$	1	1851.4807	$1s(^2S)\,2p^2(^3P)\ ^4P_{1/2}$	1	1851.1741
10	$((1s_{1/2}\,2p_{1/2})_0\,2p_{3/2})_{3/2}$	3	1851.8761	$1s(^2S)\,2p^2(^3P)\ ^4P_{3/2}$	3	1851.6101
11	$(1s_{1/2}\,(2p^2_{3/2})_2)_{5/2}$	5	1852.4077	$1s(^2S)\,2p^2(^3P)\ ^4P_{5/2}$	5	1852.2880
12	$((1s_{1/2}\,2s_{1/2})_1\,2p_{3/2})_{1/2}$	1	1853.9104	$1s(^2S)\,2s2p(^1P^o)\ ^2P^o_{1/2}$	1	1853.8947
13	$((1s_{1/2}\,2s_{1/2})_0\,2p_{3/2})_{3/2}$	3	1854.0850	$1s(^2S)\,2s2p(^1P^o)\ ^2P^o_{3/2}$	3	1854.2217
14	$((1s_{1/2}\,2p_{1/2})_1\,2p_{3/2})_{5/2}$	**5**	**1864.3543**	$1s(^2S)\,2p^2(^1D)\ ^2D_{3/2}$	**3**	**1863.9732**
15	$((1s_{1/2}\,2p_{1/2})_0\,2p_{3/2})_{3/2}$	**3**	**1864.4771**	$1s(^2S)\,2p^2(^1D)\ ^2D_{5/2}$	**5**	**1864.0761**
16	$((1s_{1/2}\,2p_{1/2})_1\,2p_{3/2})_{1/2}$	1	1867.1243	$1s(^2S)\,2p^2(^3P)\ ^2P_{1/2}$	1	1866.9400
17	$(1s_{1/2}\,(2p^2_{3/2})_2)_{3/2}$	3	1868.0803	$1s(^2S)\,2p^2(^3P)\ ^2P_{3/2}$	3	1867.8849
18	$(1s_{1/2}\,(2p^2_{3/2})_0)_{1/2}$	1	1881.3194	$1s(^2S)\,2p^2(^1S)\ ^2S_{1/2}$	1	1881.2095

NOTE— With the exception of levels 14 and 15 (marked bold) which have to be swapped in either FAC or in P08 in order for the total angular momentum J to match, this table can be used to match the *LS*- and *jj*-coupling notations. The level IDs are the same as in Figure 6.

Table 3. Center [eV] of unresolved line blends for Si and S

	Silicon					Sulfur			
Ion[a]	this work	FAC	Behar	House	Ion[a]	this work	FAC	Behar	House
Si XII (Li)	1845.02 ± 0.07	1844.67 ± 0.07	1845.83	1836.80	S XIV (Li)	2437.761 ± 0.027	2437.22 ± 0.10	2438.71	2428.21
			1845.28					2437.75	
Si XI (Be)	1827.51 ± 0.06[b]	1828.20 ± 0.18	1829.21	1819.82	S XIII (Be)	2417.51 ± 0.05[b]	2418.29 ± 0.23	2418.73	2408.40
Si X (B)	1808.39 ± 0.05	1808.38 ± 0.16	1808.93	1801.57	S XII (B)	2394.95 ± 0.05	2394.78 ± 0.18	2395.37	2386.61
			1806.30					2392.13	
Si IX (C)	1789.57 ± 0.07	1789.39 ± 0.22	1786.77	1784.72	S XI (C)	2372.81 ± 0.09	2372.12 ± 0.26	2368.82	2366.56
			1790.90					2374.27	
Si VIII (N)	1772.01 ± 0.09	1772.55 ± 0.22	1771.46	1769.43	S X (N)	2350.40 ± 0.12	2351.48 ± 0.27	2349.97	2347.74
Si VII (O)	1756.68 ± 0.08	1757.29 ± 0.21	1755.40	1755.40	S IX (O)	2332.06 ± 0.10	2332.65 ± 0.25	2330.53	2330.53
Si VI (F)	1742.03 ± 0.06[c]	1743.57 ± 0.22	1741.60	1743.31	S VIII (F)	2312.37 ± 0.09[c]	2314.97 ± 0.24	2313.57	2314.87

[a] Listed is the ion and its isoelectronic sequence in parentheses

[b] blends with a Li-like transition

[c] blends with lower charge states

NOTE—Listed are the statistical uncertainties, which are in addition to 0.13 eV (Si) and 0.23 eV (S) systematic uncertainty. A fit to the FAC models (given uncertainties derived from the fit), the energy of the strongest line according to Behar & Netzer (2002), and the lines by House (1969) averaging over the fine structure are listed as well. For O-like Si and S, Behar & Netzer (2002) and House (1969) list exactly the same value to three decimals in units of Å.

Table 4. Doppler shifts in km s^{-1} for Vela X-1

Ion	ϕ = 0.0				ϕ = 0.5	
	S02[a]	G04[b]	S02 new[c]	G04 new[c]	G04[b]	G04 new[c]
Si IX	-432 ± 173	-570^{+271}_{-490}	383 ± 173	244^{+272}_{-491}	-1028^{+275}_{-137}	-215^{+276}_{-137}
Si VIII	43 ± 214	-119^{+389}_{-488}	479 ± 214	317^{+390}_{-489}	-396	40
Si VII	-170 ± 170	-85	48 ± 170	133	-527^{+321}_{-249}	-309^{+321}_{-249}
Si VI	0 ± 211	···	-9 ± 211	···	···	···

[a] Doppler shifts from Schulz et al. (2002)

[b] Doppler shifts from Goldstein et al. (2004)

[c] Doppler shifts from S02 and G04, respectively, adjusted for the new reference energies measured at EBIT (Table 3)

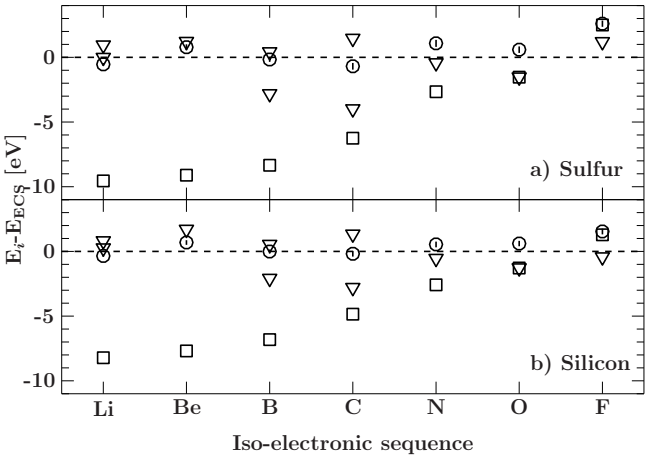

Figure 7. Deviation of the theoretical line centers in Table 3 from the centers measured with the ECS, as a function of iso-electronic sequence. While the lines derived from FAC (○) and taken from Behar & Netzer (2002, ▽) agree fairly well with our measurement, the deviation of the House (1969, □) values become significant for higher charge states.

as demonstrated below. Note that again the listed uncertainties are on the 90% confidence level and in addition to a systematic uncertainty of 0.13 eV for Si and 0.23 eV for S. For comparison, we also fitted our FAC models with Gaussians[1], and list the reference energies from Behar & Netzer (2002) and House (1969) in Table 3. Based on a similar argument, Behar & Netzer (2002) only list the strongest (photo-absorption) lines, i.e., lines with the largest oscillator strength, for the isoelectronic sequences He I to F I of the most common elements in astrophysics. According to their calculations, these lines account for more than 70%, and in most cases even more than 90%, of the absorption effect for the respective transitions. The good agreement of the energies of their principal lines with our measurements supports their argument. The House (1969) tables, on the other hand, deviate significantly from our results, especially for the higher charge states; this is probably a direct consequence of averaging over the fine structure.

To demonstrate the impact of our measurements, we use our new reference energies (Table 3) to re-determine Doppler shifts for Vela X-1 from the published wavelengths. Figure 8 shows a comparison between our laboratory Si spectra and the ones measured with *Chandra*-HETG at orbital phase $\phi_{\rm orb}$ = 0.5. Schulz et al. (2002, $\phi_{\rm orb}$ = 0.0, i.e., eclipse) and Goldstein et al. (2004, $\phi_{\rm orb}$ = 0 and $\phi_{\rm orb}$ = 0.5) both fitted the lines originating from some of the lower charge states of Si in the *Chandra* spectra, but did not model the intermediate charge states up to Li-like. Using House (1969) as a reference for the transition wavelengths resulted in Doppler shifts that not only differ between these charge states, but also deviate significantly from the He- and H-like ions in the same observation, even switching signs from blue to red-shifted (Goldstein et al. 2004). Determining the Doppler shifts based on our laboratory reference spectra (Table 4) results in Doppler shifts that are similar for all Si ions and now also agree with the Doppler shifts determined from the He- and H-like species, for which the rest-wavelengths are well known. This is more consistent with the picture of photons being reprocessed by clumps of material with an onion-like structure, where the outer layers shield the colder and denser core of the clump from the ionizing radiation of the compact object. Similar results were also obtained for Cyg X-1 (Hell et al. 2013), where these lines are seen in absorption.

5. SUMMARY

The Kα emission line energies from Si^{4+} through Si^{12+} and S^{6+} through S^{14+} have been measured using the ECS calorimeter at the LLNL EBIT facility. The results have been compared to our own FAC calculations and earlier calculations of Palmeri et al. (2008), Behar & Netzer (2002), and House (1969). The newly available data (Table 3) can directly be applied to resolve astrophysical problems such as, e.g., wind diagnostics in high mass X-ray binary systems like Vela X-1 (Liedahl & Brown 2008) and Cyg X-1 (Miškovičová et al. 2016). The 90% confidence limits of $\lesssim$ 0.5 eV on the measured line centers presented here correspond to Doppler shifts of less than 90 km s^{-1}. These measurements, therefore, provide line centers with an accuracy slightly better than the uncertainty of $\sim$ 100 km s^{-1} on the *Chandra* HETG (Mar-

[1] Note that the uncertainties on these values are derived from the fit and purely statistical

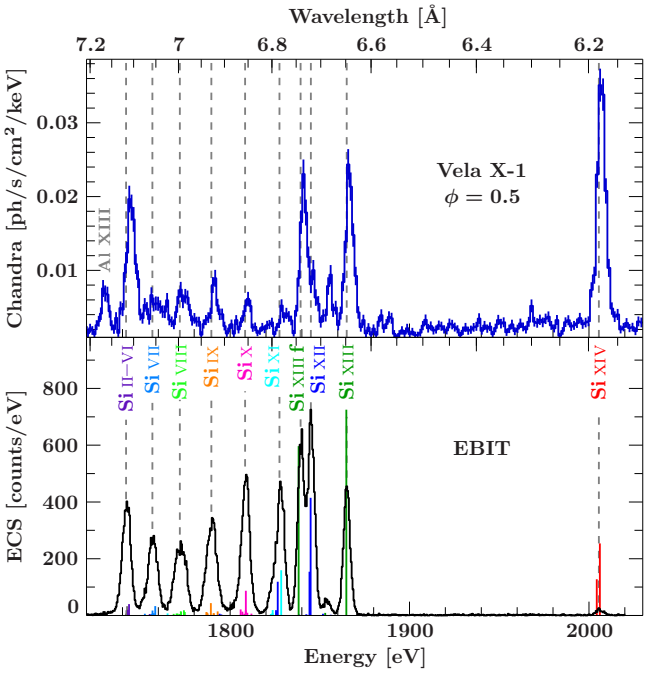

Figure 8. Comparison of the Vela X-1 Si spectral region observed by *Chandra*-HETG at orbital phase $\phi = 0.5$ (ObsID 1927) to the EBIT/ECS spectrum. The colored sticks are the transitions calculated with FAC.

shall et al. 2004; Canizares et al. 2005; Chandra X-ray Center 2015). When future missions with higher effective area make high-resolution spectra of point as well as extended celestial sources more commonly available, we expect to see these lines to be resolved in a variety of sources. Our results will then be especially useful for extended sources like supernova remnants which have yet to be observed in high resolution.

This work was performed by LLNL under the auspices of the US DOE under Contract DE-AC52-07NA27344. It was supported by NASA work orders NNX/2AH84G; by the Bundesministerium für Wirtschaft und Technologie under grant number DLR 50 OR 1113; by the European Space Agency under contract No. 4000114313/15/NL/CB; and by NASA through the Smithsonian Astrophysical Observatory (SAO) contract SV3-73016 to MIT for support of the *Chandra* X-ray Center (CXC) and Science Instruments. CXC is operated by SAO for and on the behalf of NASA under contract NAS8-03060. This research has made use of ISIS functions provided by ECAP/Remeis observatory and MIT (http://www.sternwarte.uni-erlangen.de/isis/). We thank John E. Davis for providing the `slxfig` module used for creating the presented plots. CHIANTI is a collaborative project involving George Mason University, the University of Michigan (USA) and the University of Cambridge (UK).

Software: ISIS http://space.mit.edu/asc/isis/, ISISscripts http://www.sternwarte.uni-erlangen.de/isis/, FAC v1.1.1

REFERENCES

Bautista, M. A., & Kallman, T. R. 2001, ApJS, 134, 139
Behar, E., & Netzer, H. 2002, ApJ, 570, 165
Beiersdorfer, P. 2003, ARA&A, 41, 343
—. 2008, Can. J. Phys., 86, 1
Beiersdorfer, P., Beck, B., Becker, J. A., Lepson, J. K., & Reed, K. J. 2003, in AIP Conf. Proc., Vol. 652, X-Ray and Inner-Shell Processes, ed. A. Bianconi, A. Marcelli, & N. L. Saini, 131–140
Beiersdorfer, P., Bitter, M., von Goeler, S., & Hill, K. W. 1989, Phys. Rev. A, 40, 150
Beiersdorfer, P., Phillips, T. W., Wong, K. L., Marrs, R. E., & Vogel, D. A. 1992, Phys. Rev. A, 46, 3812
Boroson, B., Vrtilek, S. D., Kallman, T., & Corcoran, M. 2003, ApJ, 592, 516
Brown, I. G., Galvin, J. E., MacGill, R. A., & Wright, R. T. 1986, Appl. Phys. Lett., 49, 1019
Calvert, J., & Tuttle, E. 1979, Il Nuovo Cimento B, 54, 413
Canizares, C. R., Davis, J. E., Dewey, D., et al. 2005, PASP, 117, 1144
Chandra X-ray Center. 2015, version 18, available online at http://cxc.harvard.edu/proposer/POG/html/index.html
Chang, C., & Cui, W. 2007, ApJ, 663, 1207
Cottam, J., Boyce, K. R., Brown, G. V., et al. 2005, in AIP Conf. Proc., Vol. 774, X-ray Diagnostics of Astrophysical Plasmas: Theory, Experiment, and Observation, ed. R. Smith, 379–382
Cowan, R. D. 1981, The Theory of Atomic Structure and Spectra (Berkeley, Los Angeles, London: University of California Press)
Decaux, V., & Beiersdorfer, P. 1993, Phys. Scr., T47, 80
Decaux, V., Beiersdorfer, P., Kahn, S. M., & Jacobs, V. L. 1997, ApJ, 482, 1076
Dere, K. P., Landi, E., Mason, H. E., Monsignori Fossi, B. C., & Young, P. R. 1997, A&AS, 125, 149
Drake, G. W. 1988, Can. J. Phys., 66, 586
Dyall, K. 1986, Comput. Phys. Commun., 39, 141
Elliott, S. R., & Marrs, R. E. 1995, Nucl. Instrum. Methods Phys. Res., Sect. B, 100, 529
Faenov, A. Y., Pikuz, S. A., & Shlyaptseva, A. S. 1994, Phys. Scr., 49, 41
Foster, A. R., Ji, L., Smith, R. K., & Brickhouse, N. S. 2012, ApJ, 756, 128
Fritz, G., Kreplin, R. W., Meekins, J. F., Unzicker, A. E., & Friedman, H. 1967, ApJ, 148, L133
Gabriel, A. H. 1972, MNRAS, 160, 99
Garcia, J. D., & Mack, J. E. 1965, Journal of the Optical Society of America, 55, 654
Goldstein, G., Huenemoerder, D. P., & Blank, D. 2004, Astron. J., 127, 2310
Gu, M. F. 2004a, FAC 1.1.1 Manual
Gu, M. F. 2004b, in AIP Conf. Proc., Vol. 730, Atomic Processes in Plasmas, ed. J. S. Cohen, D. P. Kilcrease, & S. Mazavet, 127–136
—. 2008, Can. J. Phys., 86, 675
Gu, M. F., Schmidt, M., Beiersdorfer, P., et al. 2005, ApJ, 627, 1066
Gu, M. F., Kahn, S. M., Savin, D. W., et al. 1999, ApJ, 518, 1002
Hanke, M. 2011, PhD thesis, Universität Erlangen-Nürnberg
Hanke, M., Wilms, J., Nowak, M. A., et al. 2008, PoS, MQW, 029
Hell, N., Miškovičová, I., Brown, G. V., et al. 2013, Phys. Scr., T156, 014008
Holczer, T., & Behar, E. 2012, ApJ, 747, 71
Holczer, T., Behar, E., & Kaspi, S. 2007, ApJ, 663, 799
Houck, J. C. 2002, in High Resolution X-ray Spectroscopy with XMM-Newton and Chandra, ed. G. Branduardi-Raymont, published electronically
Houck, J. C., & Denicola, L. A. 2000, in Astronomical Society of the Pacific Conference Series, Vol. 216, Astronomical Data Analysis Software and Systems IX, ed. N. Manset, C. Veillet, & D. Crabtree, 591
House, L. L. 1969, ApJS, 18, 21
Huenemoerder, D. P., Phillips, K. J. H., Sylwester, J., & Sylwester, B. 2013, ApJ, 768, 135

Kaspi, S., Brandt, W. N., George, I. M., et al. 2002, ApJ, 574, 643
Kastner, J. H., Huenemoerder, D. P., Schulz, N. S., Canizares, C. R., & Weintraub, D. A. 2002, ApJ, 567, 434
Kinkhabwala, A., Sako, M., Behar, E., et al. 2002, ApJ, 575, 732
Klapisch, M. 1971, Comput. Phys. Comm., 2, 239
Klapisch, M., Busquet, M., Bar-Shalom, A., & Oreg, J. 2006, J. Phys. IV
Landi, E., Young, P. R., Dere, K. P., Del Zanna, G., & Mason, H. E. 2013, ApJ, 763, 86
Lee, J. C., Ogle, P. M., Canizares, C. R., et al. 2001, Astrophys. J., Lett., 554, L13
Levine, M. A., Marrs, R. E., Henderson, J. R., Knapp, D. A., & Schneider, M. B. 1988, Physica Scripta Volume T, 22, 157
Liedahl, D. A., & Brown, G. V. 2008, Can. J. Phys., 86, 183
Magee, E., Beiersdorfer, P., Brown, G., & Hell, N. 2014, Rev. Sci. Instrum., 85, 11E820
Marrs, R. E., Beiersdorfer, P., & Schneider, D. 1994, Phys. Today, 47, 27
Marrs, R. E., Levine, M. A., Knapp, D. A., & Henderson, J. R. 1988, Phys. Rev. Lett., 60, 1715
Marshall, H. L., Dewey, D., & Ishibashi, K. 2004, in Proc. SPIE, Vol. 5165, X-ray and Gamma-Ray Instrumentation for Astronomy XIII, ed. K. Flanagan & O. Siegmund, 457–468
Miller, J. M., Pooley, G. G., Fabian, A. C., et al. 2012, ApJ, 757, 11
Miller, J. M., Wojdowski, P., Schulz, N. S., et al. 2005, ApJ, 620, 398
Mitsuda, K., Kelley, R. L., Boyce, K. R., et al. 2010, in Proc. SPIE, Vol. 7732, Space Telescopes and Instrumentation 2010: Ultraviolet to Gamma Ray
Miškovičová, I., Hell, N., Hanke, M., et al. 2016, A&A, accepted
Mohr, P. J., Newell, D. B., & Taylor, B. N. 2015, ArXiv e-prints, arXiv:1507.07956
Nandra, K., Barret, D., Barcons, X., et al. 2014, ATHENA: The Advanced Telescope for High ENergy Astrophysics, Mission proposal addressing *The Hot and Energetic Universe* science theme, http://sci.esa.int/jump.cfm?oid=54013
Neupert, W. M. 1971, Sol. Phys., 18, 474
Niles, A. M., Magee, E. W., Thorn, D. B., et al. 2006, Rev. Sci. Instrum., 77, 10F106
Noble, M. S., & Nowak, M. A. 2008, PASP, 120, 821
Palmeri, P., Quinet, P., Mendoza, C., et al. 2008, ApJS, 177, 408
Porter, F. S., Beiersdorfer, P., Brown, G. V., et al. 2009a, J. Phys. Conf. Series, 163, 012105
Porter, F. S., Deiker, S., Kelley, K. L., et al. 1997, in 7th International Workshop on Low-Temperature Detectors, ed. S. Cooper, 113–114
Porter, F. S., Brown, G. V., Boyce, K. R., et al. 2004, Rev. Sci. Instrum., 75, 3772
Porter, F. S., Gygax, J., Kelley, R. L., et al. 2008a, Rev. Sci. Instrum., 79, 307
Porter, F. S., Beiersdorfer, P., Brown, G. V., et al. 2008b, Journal of Low Temperature Physics, 151, 1061
Porter, F. S., Beck, B. R., Beiersdorfer, P., et al. 2008c, Can. J. Phys., 86, 231
Porter, F. S., Adams, J. S., Beiersdorfer, P., et al. 2009b, in 13th International Workshop on Low Temperature Detectors, ed. B. Young, B. Cabrera, & A. Miller, AIP Conf. Proc., 454–457
Ravera, L., Barret, D., den Herder, J. W., et al. 2014, in Proc. SPIE, Vol. 9144, Space Telescopes and Instrumentation 2014: Ultraviolet to Gamma Ray, ed. T. Takahashi, J.-W. A. den Herder, & M. Baut
Reeves, J. N., Porquet, D., Braito, V., et al. 2013, ApJ, 776, 99
Sako, M., Kahn, S. M., Paerels, F., et al. 2002, in High Resolution X-ray Spectroscopy with XMM-Newton and Chandra, ed. G. Branduardi-Raymont
Schmidt, M., Beiersdorfer, P., Chen, H., et al. 2004, ApJ, 604, 562
Schneider, M. B., Levine, M. A., Bennett, C. L., et al. 1989, in Am. Inst. Phys., Conf. Ser., Vol. 188, International symposium on electron beam ion sources and their applications, ed. A. Hershcovitch, 158–165
Schulz, N. S., Canizares, C. R., Lee, J. C., & Sako, M. 2002, Astrophys. J., Lett., 564, L21
Takahashi, T., Mitsuda, K., Kelley, R., & et al. 2010, in Proc. SPIE, Vol. 7732, Space Telescopes and Instrumentation 2010: Ultraviolet to Gamma Ray, ed. M. Arnaud, S. S. Murray, & T. Takahashi
Ullrich, A., Grübling, P., & Zschornack, G. 1998, Rev. Sci. Instrum., 69, 813
Vainshtein, L. A., & Safronova, U. I. 1985, Phys. Scr., 31, 519
Watanabe, S., Sako, M., Ishida, M., et al. 2006, ApJ, 651, 421
Yamada, C., Nagata, K., Nakamura, N., et al. 2007, J. Phys. Conf. Series, 58, 403

APPENDIX

A. OVERVIEW OVER SPECTRAL FITS

In this appendix we present the full list of measured line energies obtained with EBIT for Si (Table A1) and S (Table A2). The tables contain the best-fit values from the EBIT measurement, their identification with transitions from FAC calculations in *jj*-coupling including the calculated line energy, and, in *LS*-coupling, a comparison to calculations by P08 and database entries of CHIANTI, where available. In addition, Figures A1 and A2 give a detailed overview of the data, the best-fit including the individual Gaussian model components, and the location and theoretical relative line strengths of the transitions according to the FAC calculations.

Table A1. Identification of the fitted silicon line centers.

			jj-coupling			LS-coupling			
Key	Fit (eV)	Ion	Lower Level	Upper Level	FAC (eV)	Lower Level	Upper Level	P08 (eV)	CHIANTI
Li-1	1853.67 ± 0.20	He-like Si XIII	$1s^2$	$(1s_{1/2}\,2p_{1/2})_1$	1852.98	$1s^2\ ^1S_0$	$1s2p\ ^3P^o_1$	1853.30	1853.75
		Li-like Si XII	$1s^2\,3s_{1/2}$	$((1s_{1/2}\,2s_{1/2})_0\,3p_{3/2})_{3/2}$	1851.80	···	···	···	···
		Li-like Si XII	$1s^2\,2p_{3/2}$	$(1s_{1/2}\,(2p^2_{3/2})_0)_{1/2}$	1856.13	$1s^22p\ ^2P^o_{3/2}$	$1s(^2S)\,2p^2(^1S)\ ^2S_{1/2}$	1856.78	1854.37
Li-2	1845.09 ± 0.05	Li-like Si XII	$1s^2\,2s_{1/2}$	$((1s_{1/2}\,2s_{1/2})_0\,2p_{1/2})_{1/2}$	1844.29	$1s^22s\ ^2S_{1/2}$	$1s(^2S)\,2s2p(^3P^o)\ ^2P^o_{1/2}$	1845.11	1843.66
		Li-like Si XII	$1s^2\,2s_{1/2}$	$((1s_{1/2}\,2s_{1/2})_0\,2p_{3/2})_{3/2}$	1844.86	$1s^22s\ ^2S_{1/2}$	$1s(^2S)\,2s2p(^3P^o)\ ^2P^o_{3/2}$	1845.66	1844.21
z	1839.33 ± 0.05	He-like Si XIII	$1s^2$	$(1s_{1/2}\,2s_{1/2})_1$	1838.20	$1s^2\ ^1S_0$	$1s2s\ ^3S_1$	···	1839.42
Be-1	$1828.29^{+0.07}_{-0.08}$	Be-like Si XI	$1s^2\,2s^2$	$(1s_{1/2}\,2s^2\,2p_{3/2})_1$	1828.46	$1s^22s^2\ ^1S_0$	$1s2s^22p\ ^1P^o_1$	1828.19	···
		Li-like Si XII	$1s^2\,2s_{1/2}$	$((1s_{1/2}\,2s_{1/2})_1\,2p_{3/2})_{5/2}$	1826.55	$1s^22s\ ^2S_{1/2}$	$1s(^2S)\,2s2p(^3P^o)\ ^4P^o_{5/2}$	···	1828.19

Table A1 continued

Table A1 *(continued)*

			jj-coupling			LS-coupling			
Key	Fit (eV)	Ion	Lower Level	Upper Level	FAC (eV)	Lower Level	Upper Level	P08 (eV)	CHIANTI
Be-2	$1824.15^{+0.18}_{-0.20}$	Be-like Si XI	$1s^2\,(2s_{1/2}\,2p_{3/2})_2$	$((1s_{1/2}\,2s_{1/2})_1\,(2p^2_{3/2})_2)_2$	1823.71	$1s^22s2p\ ^3P^o_2$	$1s(^2S)\,2s2p^2(^4P)\ ^3P_2$	1823.43	···
		Be-like Si XI	$1s^2\,(2s_{1/2}\,2p_{1/2})_0$	$(((1s_{1/2}\,2s_{1/2})_0\,2p_{1/2})_{1/2}\,2p_{3/2})_1$	1823.64	$1s^22s2p\ ^3P^o_0$	$1s(^2S)\,2s^22p(^2D)\ ^3D_1$	1823.32	···
B-1	$1809.02^{+0.10}_{-0.15}$	B-like Si X	$1s^2\,2s^2\,2p_{3/2}$	$(1s_{1/2}\,2s^2\,(2p^2_{3/2})_2)_{3/2}$	1808.76	$1s^22s^22p\ ^2P^o_{3/2}$	$1s2s^22p^2\ ^2P_{3/2}$	1808.38	···
		B-like Si X	$1s^2\,2s^2\,2p_{1/2}$	$((1s_{1/2}\,2s^2\,2p_{1/2})_1\,2p_{3/2})_{1/2}$	1808.71	$1s^22s^22p\ ^2P^o_{1/2}$	$1s2s^22p^2\ ^2P_{1/2}$	1808.38	···
B-2	$1806.02^{+0.29}_{-0.49}$	B-like Si X	$1s^2\,2s^2\,2p_{3/2}$	$((1s_{1/2}\,2s^2\,2p_{1/2})_1\,2p_{3/2})_{5/2}$	1805.88	$1s^22s^22p\ ^2P^o_{3/2}$	$1s2s^22p^2\ ^2D_{5/2}$	1805.32	···
		B-like Si X	$1s^2\,2s^2\,2p_{1/2}$	$((1s_{1/2}\,2s^2\,2p_{1/2})_0\,2p_{3/2})_{3/2}$	1806.83	$1s^22s^22p\ ^2P^o_{1/2}$	$1s2s^22p^2\ ^2D_{3/2}$	1806.11	···
C-1	1794.0 ± 1.0	C-like Si IX	$1s^2\,(2s^2\,2p_{1/2}\,2p_{3/2})_2$	$(1s_{1/2}\,2s^2\,(2p^3_{3/2})_{3/2})_1$	1793.10	$1s^22s^22p^2\ ^1D_2$	$1s2s^22p^3\ ^1P^o_1$	1793.23	···
		Li-like Si XII	$1s^2\,2p_{3/2}$	$1s_{1/2}\,2s^2$	1794.18	$1s^22p\ ^2P^o_{3/2}$	$1s2s^2\ ^2S_{1/2}$	1795.26	1794.29
		Li-like Si XII	$1s^2\,2p_{1/2}$	$1s_{1/2}\,2s^2$	1795.17	$1s^22p\ ^2P^o_{1/2}$	$1s2s^2\ ^2S_{1/2}$	1796.27	1795.31
C-2	$1790.34^{+0.25}_{-0.40}$	C-like Si IX	$1s^2\,(2s^2\,2p_{1/2}\,2p_{3/2})_2$	$((1s_{1/2}\,2s^2\,2p_{1/2})_1\,(2p^2_{3/2})_2)_2$	1789.27	$1s^22s^22p^2\ ^1D_2$	$1s2s^22p^3\ ^1D^o_2$	1789.09	···
		C-like Si IX	$1s^2\,2s^2\,(2p^2_{3/2})_2$	$((1s_{1/2}\,2s^2\,2p_{1/2})_1\,(2p^2_{3/2})_0)_1$	1790.97	$1s^22s^22p^2\ ^3P_2$	$1s2s^22p^3\ ^3P^o_1$	1790.59	···
		C-like Si IX	$1s^2\,2s^2\,(2p^2_{3/2})_2$	$(1s_{1/2}\,2s^2\,(2p^3_{3/2})_{3/2})_2$	1790.81	$1s^22s^22p^2\ ^3P_2$	$1s2s^22p^3\ ^2P^o_2$	1790.41	···
C-3	$1786.85^{+0.25}_{-0.35}$	C-like Si IX	$1s^2\,2s^2\,(2p^2_{3/2})_2$	$((1s_{1/2}\,2s^2\,2p_{1/2})_1\,(2p^2_{3/2})_2)_3$	1786.83	$1s^22s^22p^2\ ^3P_2$	$1s2s^22p^3\ ^3D^o_3$	1786.26	···
		C-like Si IX	$1s^2\,2s^2\,(2p^2_{3/2})_0$	$(1s_{1/2}\,2s^2\,(2p^3_{3/2})_{3/2})_1$	1786.98	$1s^22s^22p^2\ ^1S_0$	$1s2s^22p^3\ ^1P^o_1$	1786.88	···
		C-like Si IX	$1s^2\,(2s^2\,2p_{1/2}\,2p_{3/2})_1$	$((1s_{1/2}\,2s^2\,2p_{1/2})_0\,(2p^2_{3/2})_2)_2$	1787.43	$1s^22s^22p^2\ ^3P_1$	$1s2s^22p^3\ ^3D^o_2$	1786.67	···
N-1	$1774.29^{+0.20}_{-0.19}$	N-like Si VIII	$1s^2\,2s^2\,(2p_{1/2}\,(2p^2_{3/2})_2)_{5/2}$	$((1s_{1/2}\,2s^2\,2p_{1/2})_1\,(2p^3_{3/2})_{3/2})_{3/2}$	1774.25	$1s^22s^22p^3\ ^2D^o_{5/2}$	$1s2s^22p^4\ ^2P_{3/2}$	1773.66	···
		N-like Si VIII	$1s^2\,2s^2\,(2p_{1/2}\,(2p^2_{3/2})_2)_{3/2}$	$((1s_{1/2}\,2s^2\,2p_{1/2})_1\,(2p^3_{3/2})_{3/2})_{1/2}$	1774.74	$1s^22s^22p^3\ ^2D^o_{3/2}$	$1s2s^22p^4\ ^2P_{1/2}$	1774.19	···
		N-like Si VIII	$1s^2\,2s^2\,(2p^3_{3/2})_{3/2}$	$(1s_{1/2}\,2s^2\,(2p^2_{3/2})_0)_{1/2}$	1774.47	$1s^22s^22p^3\ ^2P^o_{3/2}$	$1s2s^22p^4\ ^2S_{1/2}$	1773.86	···
N-2	$1770.5^{+0.5}_{-4.9}$	N-like Si VIII	$1s^2\,2s^2\,(2p^2_{3/2})_{3/2}$	$((1s_{1/2}\,2s^2\,2p_{1/2})_1\,(2p^3_{3/2})_{3/2})_{3/2}$	1770.21	$1s^22s^22p^3\ ^2P^o_{3/2}$	$1s2s^22p^4\ ^2P_{3/2}$	1769.46	···
		N-like Si VIII	$1s^2\,2s^2\,(2p_{1/2}\,(2p^2_{3/2})_0)_{1/2}$	$((1s_{1/2}\,2s^2\,2p_{1/2})_1\,(2p^3_{3/2})_{3/2})_{1/2}$	1770.74	$1s^22s^22p^3\ ^2P^o_{1/2}$	$1s2s^22p^4\ ^2P_{1/2}$	1770.01	···
		N-like Si VIII	$1s^2\,2s^2\,(2p_{1/2}\,(2p^2_{3/2})_2)_{5/2}$	$((1s_{1/2}\,2s^2\,2p_{1/2})_1\,(2p^3_{3/2})_{3/2})_{5/2}$	1772.56	$1s^22s^22p^3\ ^2D^o_{5/2}$	$1s2s^22p^4\ ^2D_{5/2}$	1771.78	···
		N-like Si VIII	$1s^2\,2s^2\,(2p_{1/2}\,(2p^2_{3/2})_2)_{3/2}$	$(1s_{1/2}\,2s^2\,2p^2_{1/2}\,(2p^2_{3/2})_2)_{3/2}$	1172.66	$1s^22s^22p^3\ ^2D^o_{3/2}$	$1s2s^22p^4\ ^2D_{3/2}$	1771.76	···
		N-like Si VIII	$1s^2\,2s^2\,(2p_{1/2}\,(2p^2_{3/2})_2)_{3/2}$	$((1s_{1/2}\,2s^2\,2p_{1/2})_0\,(2p^3_{3/2})_{3/2})_{3/2}$	1172.02	$1s^22s^22p^3\ ^4S^o_{3/2}$	$1s2s^22p^4\ ^4P_{3/2}$	1770.60	···
N-3	$1766.9^{+1.0}_{-1.3}$	N-like Si VIII	$1s^2\,2s^2\,(2p^2_{3/2})_{3/2}$	$((1s_{1/2}\,2s^2\,2p_{1/2})_1\,(2p^3_{3/2})_{3/2})_{5/2}$	1768.52	$1s^22s^22p^3\ ^2P^o_{3/2}$	$1s2s^22p^4\ ^2D_{5/2}$	1767.59	···
		Be-like Si XI	$1s^2\,(2p_{1/2}\,2p_{3/2})_2$	$(1s_{1/2}\,2s^2\,2p_{3/2})_1$	1765.18	$1s^22p^2\ ^1D_2$	$1s2s^22p\ ^1P^o_1$	1766.01	···
O-1	1758.7 ± 0.5	O-like Si VII	$1s^2\,2s^2\,(2p_{1/2}\,(2p^3_{3/2})_{3/2})_2$	$(1s_{1/2}\,2s^2\,2p^2_{1/2}\,(2p^3_{3/2})_{3/2})_1$	1758.28	$1s^22s^22p^4\ ^1D_2$	$1s2s^22p^5\ ^1P^o_1$	1756.35	···
O-2	1756.0 ± 0.4	O-like Si VII	$1s^2\,2s^2\,2p^2_{1/2}\,(2p^2_{3/2})_2$	$(1s_{1/2}\,2s^2\,2p^2_{1/2}\,(2p^3_{3/2})_{3/2})_2$	1756.79	$1s^22s^22p^4\ ^3P_2$	$1s2s^22p^5\ ^3P^o_2$	1754.39	···
		O-like Si VII	$1s^2\,2s^2\,2p^2_{1/2}\,(2p^2_{3/2})_2$	$(1s_{1/2}\,2s^2\,2p_{1/2}\,2p^4_{3/2})_1$	1757.38	$1s^22s^22p^4\ ^3P_0$	$1s2s^22p^5\ ^3P^o_1$	1754.96	···
		O-like Si VII	$1s^2\,2s^2\,(2p_{1/2}\,(2p^3_{3/2})_{3/2})_1$	$(1s_{1/2}\,2s^2\,2p_{1/2}\,2p^4_{3/2})_0$	1757.32	$1s^22s^22p^4\ ^3P_1$	$1s2s^22p^5\ ^3P^o_0$	1754.78	···
		O-like Si VII	$1s^2\,2s^2\,(2p_{1/2}\,(2p^3_{3/2})_{3/2})_1$	$(1s_{1/2}\,2s^2\,2p^2_{1/2}\,(2p^3_{3/2})_{3/2})_2$	1756.30	$1s^22s^22p^4\ ^3P_1$	$1s2s^22p^5\ ^3P^o_2$	1753.91	···
		O-like Si VII	$1s^2\,2s^2\,2p^4_{3/2}$	$(1s_{1/2}\,2s^2\,2p_{1/2}\,2p^4_{3/2})_1$	1756.70	$1s^22s^22p^4\ ^3P_0$	$1s2s^22p^5\ ^3P^o_1$	1754.29	···
O-3	1751.4 ± 0.6	O-like Si VII	$1s^2\,2s^2\,2p^2_{1/2}\,(2p^2_{3/2})_0$	$(1s_{1/2}\,2s^2\,2p^2_{1/2}\,(2p^3_{3/2})_{3/2})_1$	1752.47	$1s^22s^22p^4\ ^1S_0$	$1s2s^22p^5\ ^1P^o_1$	1750.40	···
F-1	$1742.88^{+0.15}_{-0.17}$	F-like Si VI	$1s^2\,2s^2\,2p^2_{1/2}\,(2p^3_{3/2})_{3/2}$	$1s_{1/2}\,2s^2\,2p^6$	1743.71	$1s^22s^22p^5\ ^2P^o_{3/2}$	$1s2s^22p^6\ ^2S_{1/2}$	1740.79	···
		F-like Si VI	$1s^2\,2s^2\,2p_{1/2}\,2p^4_{3/2}$	$1s_{1/2}\,2s^2\,2p^6$	1743.09	$1s^22s^22p^5\ ^2P^o_{1/2}$	$1s2s^22p^6\ ^2S_{1/2}$	1740.15	···
		Ne-like Si V	$1s^2\,2s^2\,2p^2_{1/2}\,((2p^3_{3/2})_{3/2}\,3s_{1/2})_1$	$(1s_{1/2}\,2s^2\,2p^6\,3s_{1/2})_1$	1742.23	$1s^22s^22p^5 3s\ ^3P^o_1$	$1s2s^22p^6 3s\ ^3S_1$	1743.06	···
		Ne-like Si V	$1s^2\,2s^2\,(2p_{1/2}\,2p^4_{3/2}\,3s_{1/2})_1$	$(1s_{1/2}\,2s^2\,2p^6\,3s_{1/2})_0$	1742.44	$1s^22s^22p^5 3s\ ^1P^o_1$	$1s2s^22p^6 3s\ ^1S_0$	1743.33	···
		Ne-like Si V	$1s^2\,2s^2\,2p^2_{1/2}\,((2p^3_{3/2})_{3/2}\,3s_{1/2})_2$	$(1s_{1/2}\,2s^2\,2p^6\,3s_{1/2})_1$	1742.56	$1s^22s^22p^5 3s\ ^3P^o_2$	$1s2s^22p^6 3s\ ^3S_1$	1743.38	···
X-1	$1740.04^{+0.27}_{-0.36}$	Na–Si-like Si I–IV	···	···	···				

NOTE—Identification of the fitted Si lines with transitions of the FAC simulation. The first column is the key to the line labels in Figure A1, the third column indicates the ionization state. For the He-like lines the key of Gabriel (1972) is used. Columns 4–6 show the identification with FAC lines, columns 7–9 the corresponding transitions from Palmeri et al. (2008). Note that these calculated transition wavelengths listed by P08 have been empirically shifted by P08 for ions with $3 \le N \le 9$, where N is the number of electrons. Statistical uncertainties are shown as 90 % confidence intervals. There is an additional systematic uncertainty of 0.13 eV on all lines.

Table A2. Identification of the fitted sulfur line centers.

			jj-coupling			LS-coupling			
Key	Fit (eV)	Ion	Lower Level	Upper Level	FAC (eV)	Lower Level	Upper Level	P08 (eV)	CHIANTI
Li-1	2450 ± 1.0	Li-like S XIV	$1s^2\ 2p_{3/2}$	$(1s_{1/2}\,(2p^2_{3/2})_0)_{1/2}$	2449.95	$1s^2 2p\ ^2P^o_{3/2}$	$1s(^2S)\,2p^2(^1S)\,^2S_{1/2}$	2450.67	2449.26
		Li-like S XIV	$1s^2\ 2p_{1/2}$	$(1s_{1/2}\,(2p^2_{3/2})_0)_{1/2}$	2451.78	$1s^2 2p\ ^2P^o_{1/2}$	$1s(^2S)\,2p^2(^1S)\,^2S_{1/2}$	2452.51	2451.15
Li-2	$2447.02^{+0.19}_{-0.27}$	Li-like S XIV	$1s^2\ 2s_{1/2}$	$((1s_{1/2}\,2s_{1/2})_1\,2p_{3/2})_{1/2}$	2447.65	$1s^2 2s\ ^2S_{1/2}$	$1s(^2S)\,2s2p(^1P^o)\,^2P^o_{1/2}$	2448.01	2447.04
		He-like S XV	$1s^2$	$(1s_{1/2}\,2p_{1/2})_1$	2446.32	$1s^2\ ^1S_0$	$1s2p\ ^3P^o_1$	2446.65	2447.14
Li-3	$2437.797^{+0.023}_{-0.024}$	Li-like S XIV	$1s^2\ 2s_{1/2}$	$((1s_{1/2}\,2s_{1/2})_0\,2p_{1/2})_{1/2}$	2436.55	$1s^2 2s\ ^2S_{1/2}$	$1s(^2S)\,2s2p(^3P^o)\,^2P^o_{1/2}$	2437.52	2437.04
		Li-like S XIV	$1s^2\ 2s_{1/2}$	$((1s_{1/2}\,2s_{1/2})_0\,2p_{3/2})_{3/2}$	2437.58	$1s^2 2s\ ^2S_{1/2}$	$1s(^2S)\,2s2p(^3P^o)\,^2P^o_{3/2}$	2438.47	2437.99
z	$2430.380^{+0.024}_{-0.019}$	He-like S XV	$1s^2$	$(1s_{1/2}\,2s_{1/2})_1$	2429.08	$1s^2\ ^1S_0$	$1s2s\ ^3S_1$	⋯	2430.35
Be-1	$2418.51^{+0.10}_{-0.09}$	Be-like S XIII	$1s^2\ 2s^2$	$(1s_{1/2}\,2s^2\,2p_{3/2})_1$	2418.38	$1s^2 2s^2\ ^1S_0$	$1s2s^2 2p\ ^1P^o_1$	2418.45	⋯
Be-2	$2414.7^{+1.0}_{-4.0}$	Li-like S XIV	$1s^2\ 2s_{1/2}$	$((1s_{1/2}\,2s_{1/2})_1\,2p_{3/2})_{5/2}$	2416.26	$1s^2 2s\ ^2S_{1/2}$	$1s(^2S)\,2s2p(^3P^o)\,^4P^o_{5/2}$	⋯	2416.99
		Li-like S XIV	$1s^2\ 2s_{1/2}$	$((1s_{1/2}\,2s_{1/2})_1\,2p_{1/2})_{1/2}$	2414.51	$1s^2 2s\ ^2S_{1/2}$	$1s(^2S)\,2s2p(^3P^o)\,^4P^o_{1/2}$	2414.92	2415.24
		Li-like S XIV	$1s^2\ 2s_{1/2}$	$((1s_{1/2}\,2s_{1/2})_1\,2p_{1/2})_{3/2}$	2415.02	$1s^2 2s\ ^2S_{1/2}$	$1s(^2S)\,2s2p(^3P^o)\,^4P^o_{3/2}$	2415.67	2415.76
Be-3	$2412.0^{+0.8}_{-1.4}$	Be-like S XIII	$1s^2\,(2s_{1/2}\,2p_{3/2})_2$	$((1s_{1/2}\,2s_{1/2})_1\,(2p^2_{3/2})_2)_2$	2412.83	$1s^2 2s2p\ ^3P^o_2$	$1s(^2S)\,2s2p^2(^4P)\,^3P_2$	2412.89	⋯
		Be-like S XIII	$1s^2\,(2s_{1/2}\,2p_{1/2})_0$	$(((1s_{1/2}\,2s_{1/2})_1\,2p_{1/2})_{1/2}\,2p_{3/2})_1$	2412.82	$1s^2 2s2p\ ^3P^o_0$	$1s(^2S)\,2s2p(^2D)\,^3D_1$	2412.75	⋯
B-1	$2395.51^{+0.06}_{-0.10}$	B-like S XII	$1s^2\,2s^2\,2p_{3/2}$	$(1s_{1/2}\,2s^2\,(2p^2_{3/2})_2)_{3/2}$	2395.25	$1s^2 2s^2 2p\ ^2P^o_{3/2}$	$1s2s^2 2p^2\ ^2P_{3/2}$	2394.90	⋯
		B-like S XII	$1s^2\,2s^2\,2p_{1/2}$	$((1s_{1/2}\,2s^2\,2p_{1/2})_1\,2p_{3/2})_{1/2}$	2395.11	$1s^2 2s^2 2p\ ^2P^o_{1/2}$	$1s2s^2 2p^2\ ^2P_{1/2}$	2394.86	⋯
		B-like S XII	$1s^2\,2s^2\,2p_{1/2}$	$((1s_{1/2}\,2s^2\,2p_{1/2})_1\,2p_{3/2})_{1/2}$	2396.87	$1s^2 2s^2 2p\ ^2P^o_{1/2}$	$1s2s^2 2p^2\ ^2P_{3/2}$	2396.52	⋯
B-2	$2391.36^{+0.20}_{-0.42}$	B-like S XII	$1s^2\,2s^2\,2p_{3/2}$	$((1s_{1/2}\,2s^2\,2p_{1/2})_1\,2p_{3/2})_{5/2}$	2391.41	$1s^2 2s^2 2p\ ^2P^o_{3/2}$	$1s2s^2 2p^2\ ^2D_{5/2}$	2390.87	⋯
		B-like S XII	$1s^2\,2s^2\,2p_{1/2}$	$((1s_{1/2}\,2s^2\,2p_{1/2})_0\,2p_{3/2})_{3/2}$	2393.07	$1s^2 2s^2 2p\ ^2P^o_{1/2}$	$1s2s^2 2p^2\ ^2D_{3/2}$	2392.27	⋯
		B-like S XII	$1s^2\,2s^2\,2p_{3/2}$	$((1s_{1/2}\,2s^2\,2p_{1/2})_1\,2p_{3/2})_{1/2}$	2393.50	$1s^2 2s^2 2p\ ^2P^o_{3/2}$	$1s2s^2 2p^2\ ^2P_{1/2}$	2393.24	⋯
C-1	$2378.26^{+0.27}_{-0.20}$	C-like S XI	$1s^2\,2s^2\,(2p_{1/2}\,2p_{3/2})_2$	$(1s_{1/2}\,2s^2\,(2p^3_{3/2})_{3/2})_1$	2376.60	$1s^2 2s^2 2p^2\ ^1D_2$	$1s2s^2 2p^3\ ^1P^o_1$	2376.59	⋯
		Li-like S XIV	$1s^2\ 2p_{3/2}$	$1s_{1/2}\,2s^2$	2377.32	$1s^2 2p\ ^2P^o_{3/2}$	$1s2s^2\ ^2S_{1/2}$	2378.50	2378.32
		Li-like S XIV	$1s^2\ 2p_{1/2}$	$1s_{1/2}\,2s^2$	2379.16	$1s^2 2p\ ^2P^o_{1/2}$	$1s2s^2\ ^2S_{1/2}$	2380.37	2380.19
C-2	$2373.25^{+0.14}_{-0.16}$	C-like S XI	$1s^2\,2s^2\,(2p_{1/2}\,2p_{3/2})_2$	$((1s_{1/2}\,2s^2\,2p_{1/2})_1\,(2p^2_{3/2})_2)_2$	2371.92	$1s^2 2s^2 2p^2\ ^1D_2$	$1s2s^2 2p^3\ ^1D^o_2$	2371.59	⋯
		C-like S XI	$1s^2\,2s^2\,(2p^2_{3/2})_2$	$((1s_{1/2}\,2s^2\,2p_{1/2})_1\,(2p^2_{3/2})_0)_1$	2373.92	$1s^2 2s^2 2p^2\ ^3P_2$	$1s2s^2 2p^3\ ^3P^o_1$	2373.36	⋯
		C-like S XI	$1s^2\,2s^2\,(2p_{1/2}\,2p_{3/2})_1$	$((1s_{1/2}\,2s^2\,2p_{1/2})_1\,(2p^2_{3/2})_2)_1$	2373.23	$1s^2 2s^2 2p^2\ ^3P_1$	$1s2s^2 2p^3\ ^3S^o_1$	2372.77	⋯
		C-like S XI	$1s^2\,2s^2\,(2p^2_{3/2})_2$	$(1s_{1/2}\,2s^2\,(2p^3_{3/2})_{3/2})_2$	2373.52	$1s^2 2s^2 2p^2\ ^3P_2$	$1s2s^2 2p^3\ ^3P^o_2$	2372.95	⋯
C-3	$2368.83^{+0.20}_{-0.24}$	C-like S XI	$1s^2\,2s^2\,(2p^2_{3/2})_2$	$((1s_{1/2}\,2s^2\,2p_{1/2})_1\,(2p^2_{3/2})_2)_3$	2368.58	$1s^2 2s^2 2p^2\ ^3P_2$	$1s2s^2 2p^3\ ^3D^o_3$	2367.83	⋯
		C-like S XI	$1s^2\,2s^2\,(2p_{1/2}\,2p_{3/2})_1$	$((1s_{1/2}\,2s^2\,2p_{1/2})_0\,(2p^2_{3/2})_2)_2$	2369.55	$1s^2 2s^2 2p^2\ ^3P_1$	$1s2s^2 2p^3\ ^3D^o_2$	2368.55	⋯
		C-like S XI	$1s^2\,2s^2\,(2p^2_{3/2})_0$	$(1s_{1/2}\,2s^2\,(2p^3_{3/2})_{3/2})_1$	2369.14	$1s^2 2s^2 2p^2\ ^1S_0$	$1s2s^2 2p^3\ ^1P^o_1$	2368.87	⋯
N-1	$2354.33^{+0.23}_{-0.29}$	N-like S X	$1s^2\,2s^2\,(2p_{1/2}\,(2p^2_{3/2})_2)_{5/2}$	$((1s_{1/2}\,2s^2\,2p_{1/2})_1\,(2p^3_{3/2})_{3/2})_{3/2}$	2353.74	$1s^2 2s^2 2p^3\ ^2D^o_{5/2}$	$1s2s^2 2p^4\ ^2P_{3/2}$	2352.86	⋯
		N-like S X	$1s^2\,2s^2\,(2p_{1/2}\,(2p^2_{3/2})_2)_{3/2}$	$((1s_{1/2}\,2s^2\,2p_{1/2})_1\,(2p^3_{3/2})_{3/2})_{1/2}$	2354.57	$1s^2 2s^2 2p^3\ ^2D^o_{3/2}$	$1s2s^2 2p^4\ ^2P_{1/2}$	2353.85	⋯
		N-like S X	$1s^2\,2s^2\,(2p^3_{3/2})_{3/2}$	$1s_{1/2}\,2s^2\,2p^4_{3/2}$	2353.80	$1s^2 2s^2 2p^3\ ^2P^o_{3/2}$	$1s2s^2 2p^4\ ^2S_{1/2}$	2352.91	⋯
N-2	$2349.94^{+0.23}_{-0.32}$	N-like S X	$1s^2\,2s^2\,(2p_{1/2}\,(2p^2_{3/2})_2)_{5/2}$	$((1s_{1/2}\,2s^2\,2p_{1/2})_1\,(2p^3_{3/2})_{3/2})_{5/2}$	2351.45	$1s^2 2s^2 2p^3\ ^2D^o_{5/2}$	$1s2s^2 2p^4\ ^2D_{5/2}$	2350.45	⋯
		N-like S X	$1s^2\,2s^2\,(2p_{1/2}\,(2p^2_{3/2})_2)_{3/2}$	$(1s_{1/2}\,2s^2\,2p^2_{1/2}\,(2p^2_{3/2})_2)_{3/2}$	2351.61	$1s^2 2s^2 2p^3\ ^2D^o_{3/2}$	$1s2s^2 2p^4\ ^2D_{3/2}$	2350.37	⋯
		N-like S X	$1s^2\,2s^2\,(2p_{1/2}\,(2p^2_{3/2})_0)_{1/2}$	$((1s_{1/2}\,2s^2\,2p_{1/2})_1\,(2p^3_{3/2})_{3/2})_{1/2}$	2349.55	$1s^2 2s^2 2p^3\ ^2P^o_{1/2}$	$1s2s^2 2p^4\ ^2P_{1/2}$	2348.59	⋯
		N-like S X	$1s^2\,2s^2\,(2p^3_{3/2})_{3/2}$	$((1s_{1/2}\,2s^2\,2p_{1/2})_1\,(2p^3_{3/2})_{3/2})_{3/2}$	2348.63	$1s^2 2s^2 2p^3\ ^2P^o_{3/2}$	$1s2s^2 2p^4\ ^2P_{3/2}$	2347.61	⋯
		N-like S X	$1s^2\,2s^2\,(2p_{1/2}\,(2p^2_{3/2})_2)_{3/2}$	$((1s_{1/2}\,2s^2\,2p_{1/2})_0\,(2p^3_{3/2})_{3/2})_{3/2}$	2350.86	$1s^2 2s^2 2p^3\ ^4S^o_{3/2}$	$1s2s^2 2p^4\ ^4P_{3/2}$	2349.12	⋯
		N-like S X	$1s^2\,2s^2\,(2p_{1/2}\,(2p^2_{3/2})_2)_{3/2}$	$(1s_{1/2}\,2s^2\,2p^2_{1/2}\,(2p^2_{3/2})_2)_{5/2}$	2349.70	$1s^2 2s^2 2p^3\ ^4S^o_{3/2}$	$1s2s^2 2p^4\ ^4P_{5/2}$	2348.10	⋯
N-3	$2345.6^{+0.4}_{-0.6}$	N-like S X	$1s^2\,2s^2\,(2p^3_{3/2})_{3/2}$	$((1s_{1/2}\,2s^2\,2p_{1/2})_1\,(2p^3_{3/2})_{3/2})_{5/2}$	2346.34	$1s^2 2s^2 2p^3\ ^2P^o_{3/2}$	$1s2s^2 2p^4\ ^2D_{5/2}$	2345.17	⋯
		Be-like S XIII	$1s^2\,(2p_{1/2}\,2p_{3/2})_2$	$(1s_{1/2}\,2s^2\,2p_{3/2})_1$	2343.42	$1s^2 2p^2\ ^1D_2$	$1s2s^2 2p\ ^1P^o_1$	2344.54	⋯
O-1	$2335.6^{+0.5}_{-4.3}$	O-like S IX	$1s^2\,2s^2\,(2p_{1/2}\,(2p^3_{3/2})_{3/2})_2$	$(1s_{1/2}\,2s^2\,2p^2_{1/2}\,(2p^3_{3/2})_{3/2})_1$	2333.91	$1s^2 2s^2 2p^4\ ^1D_2$	$1s2s^2 2p^5\ ^1P^o_1$	2331.76	⋯
O-2	$2331.82^{+0.27}_{-0.48}$	O-like S IX	$1s^2\,2s^2\,2p^2_{1/2}\,(2p^2_{3/2})_2$	$(1s_{1/2}\,2s^2\,2p^2_{1/2}\,(2p^3_{3/2})_{3/2})_2$	2331.82	$1s^2 2s^2 2p^4\ ^3P_2$	$1s2s^2 2p^5\ ^3P^o_2$	2329.13	⋯
		O-like S IX	$1s^2\,2s^2\,2p^2_{1/2}\,(2p^2_{3/2})_2$	$(1s_{1/2}\,2s^2\,2p_{1/2}\,2p^4_{3/2})_1$	2332.91	$1s^2 2s^2 2p^4\ ^3P_2$	$1s2s^2 2p^5\ ^3P^o_1$	2330.18	⋯
		O-like S IX	$1s^2\,2s^2\,(2p_{1/2}\,(2p^3_{3/2})_{3/2})_1$	$(1s_{1/2}\,2s^2\,2p_{1/2}\,2p^4_{3/2})_0$	2332.76	$1s^2 2s^2 2p^4\ ^3P_1$	$1s2s^2 2p^5\ ^3P^o_0$	2329.83	⋯
		O-like S IX	$1s^2\,2s^2\,(2p_{1/2}\,(2p^3_{3/2})_{3/2})_1$	$(1s_{1/2}\,2s^2\,2p^2_{1/2}\,(2p^3_{3/2})_{3/2})_2$	2330.84	$1s^2 2s^2 2p^4\ ^3P_1$	$1s2s^2 2p^5\ ^3P^o_2$	2328.21	⋯
		O-like S IX	$1s^2\,2s^2\,2p^4_{3/2}$	$(1s_{1/2}\,2s^2\,2p_{1/2}\,2p^4_{3/2})_1$	2331.61	$1s^2 2s^2 2p^4\ ^3P_0$	$1s2s^2 2p^5\ ^3P^o_1$	2328.91	⋯
O-3	$2327.2^{+0.5}_{-0.7}$	O-like S IX	$1s^2\,2s^2\,2p^2_{1/2}\,(2p^2_{3/2})_0$	$(1s_{1/2}\,2s^2\,2p^2_{1/2}\,(2p^3_{3/2})_{3/2})_1$	2316.67	$1s^2 2s^2 2p^4\ ^1S_0$	$1s2s^2 2p^5\ ^1P^o_1$	2324.33	⋯
F-1	$2315.00^{+0.17}_{-0.24}$	F-like S VIII	$1s^2\,2s^2\,2p^2_{1/2}\,(2p^3_{3/2})_{3/2}$	$1s_{1/2}\,2s^2\,2p^6$	2315.36	$1s^2 2s^2 2p^5\ ^2P^o_{3/2}$	$1s2s^2 2p^6\ ^2S_{1/2}$	2312.40	⋯

Table A2 continued

Table A2 *(continued)*

Key	Fit (eV)	Ion	jj-coupling		FAC (eV)	LS-coupling		P08 (eV)	CHIANTI
			Lower Level	Upper Level		Lower Level	Upper Level		
		F-like S VIII	$1s^2\,2s^2\,2p_{1/2}\,2p_{3/2}^4$	$1s_{1/2}\,2s^2\,2p^6$	2314.13	$1s^2 2s^2 2p^5\ {}^2P^o_{1/2}$	$1s2s^2 2p^6\ {}^2S_{1/2}$	2311.15	···
		Ne-like S VII	$1s^2\,2s^2\,2p_{1/2}^2\,((2p_{3/2}^3)_{3/2}\,3s_{1/2})_2$	$(1s_{1/2}\,2s^2\,2p_{1/2}^2\,2p_{3/2}^4\,3s_{1/2})_1$	2313.58	$1s^2 2s^2 2p^5 3s\ {}^3P^o_2$	$1s2s^2 2p^6 3s\ {}^3S_1$	2314.74	···
		Ne-like S VII	$1s^2\,2s^2\,2p_{1/2}^2\,((2p_{3/2}^3)_{3/2}\,3s_{1/2})_1$	$(1s_{1/2}\,2s^2\,2p_{1/2}^2\,2p_{3/2}^4\,3s_{1/2})_1$	2312.99	$1s^2 2s^2 2p^5 3s\ {}^3P^o_1$	$1s2s^2 2p^6 3s\ {}^3S_1$	2314.17	···
		Ne-like S VII	$1s^2\,2s^2\,(2p_{1/2}\,2p_{3/2}^4\,3s_{1/2})_1$	$(1s_{1/2}\,2s^2\,2p_{1/2}^2\,2p_{3/2}^4\,3s_{1/2})_0$	2313.35	$1s^2 2s^2 2p^5 3s\ {}^1P^o_1$	$1s2s^2 2p^6 3s\ {}^1S_0$	2312.62	···
F-2	$2311.22^{+0.27}_{+0.41}$	Na-like S VI	$1s^2\,2s^2\,((2p_{1/2}\,2p_{3/2}^4\,3s_{1/2})_1\,3p_{3/2})_{5/2}$	$((1s_{1/2}\,2s^2\,2p_{1/2}^2\,2p_{3/2}^4\,3s_{1/2})_0\,3p_{3/2})_{3/2}$	2311.62	$1s^2 2s^2 2p^5 3s 3p\ {}^2D_{5/2}$	$1s2s^2 2p^6 3s 3p\ {}^2P^o_{3/2}$	2312.71	···
		B-like S XII	$1s^2\,(2p_{1/2}\,(2p_{3/2}^2)_2)_{5/2}$	$(1s_{1/2}\,2s^2\,(2p_{3/2}^2)_2)_{3/2}$	2309.50	$1s^2 2p^3\ {}^2D^o_{5/2}$	$1s2s^2 2p^2\ {}^2P_{3/2}$	2310.12	···
		Na–S-like S I–VI	···	···	···				
F-3	$2306.9^{+0.4}_{-0.7}$	B-like S XII	$1s^2\,(2p_{1/2}\,(2p_{3/2}^2)_2)_{3/2}$	$((1s_{1/2}\,2s^2\,2p_{1/2})_1\,2p_{3/2})_{1/2}$	2307.79	$1s^2 2p^3\ {}^2D^o_{3/2}$	$1s2s^2 2p^2\ {}^2P_{1/2}$	2308.57	···
		B-like S XII	$1s^2\,(2p_{1/2}\,(2p_{3/2}^2)_2)_{5/2}$	$((1s_{1/2}\,2s^2\,2p_{1/2})_1\,2p_{3/2})_{5/2}$	2305.65	$1s^2 2p^3\ {}^2D^o_{5/2}$	$1s2s^2 2p^2\ {}^2D_{5/2}$	2306.12	···
		B-like S XII	$1s^2\,(2p_{1/2}\,(2p_{3/2}^2)_2)_{3/2}$	$(1s_{1/2}\,2s^2\,(2p_{3/2}^2)_2)_{5/2}$	2304.74	$1s^2 2p^3\ {}^4S^o_{3/2}$	$1s2s^2 2p^2\ {}^4P_{5/2}$	2303.85	···

NOTE—Identification of the fitted S lines with transitions of the FAC simulation. The first column is the key to the line labels in Figure A1, the third column indicates the ionization state. For the He-like lines the key of Gabriel (1972) is used. Columns 4–6 show the identification with FAC lines, columns 7–9 the corresponding transitions from Palmeri et al. (2008). Note that these calculated transition wavelengths listed by P08 have been empirically shifted by P08 for ions with $3 \le N \le 9$, where N is the number of electrons. Statistical uncertainties are given as 90% confidence intervals. There is an additional systematic uncertainty of 0.23 eV on all lines.

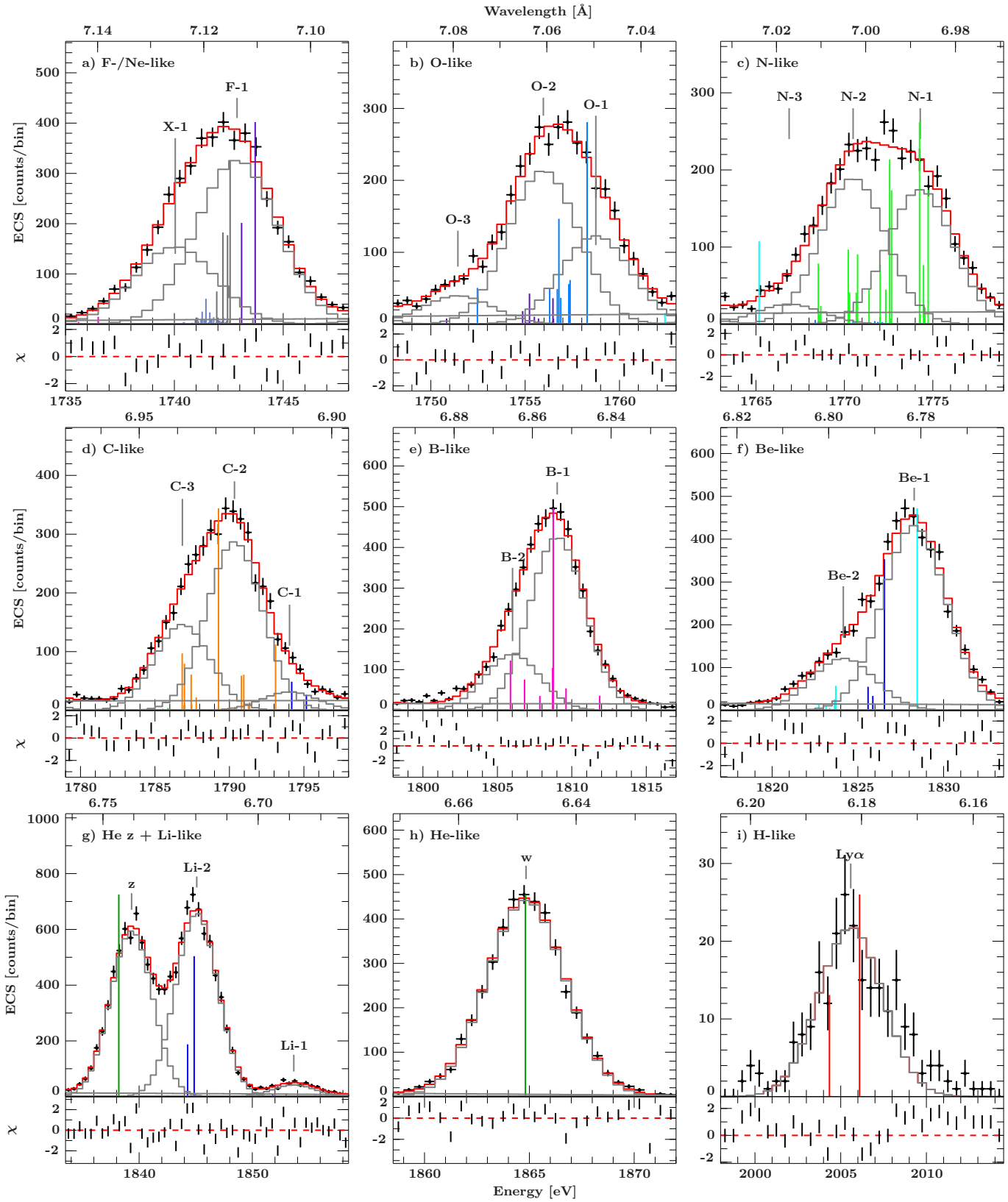

Figure A1. Fit of the measured Si Kα spectrum. The data are shown in black, the red line shows the model, model components are shown as gray lines. Vertical lines represent the theoretical predictions according to FAC, color-coded for charge states (see Figure 1). The FAC lines are renormalized such that the strongest FAC line in each panel matches the highest peak, i.e., relative FAC line strengths are preserved within but not between panels. Line labels can be used as an identifier for the transitions listed in Table A1.

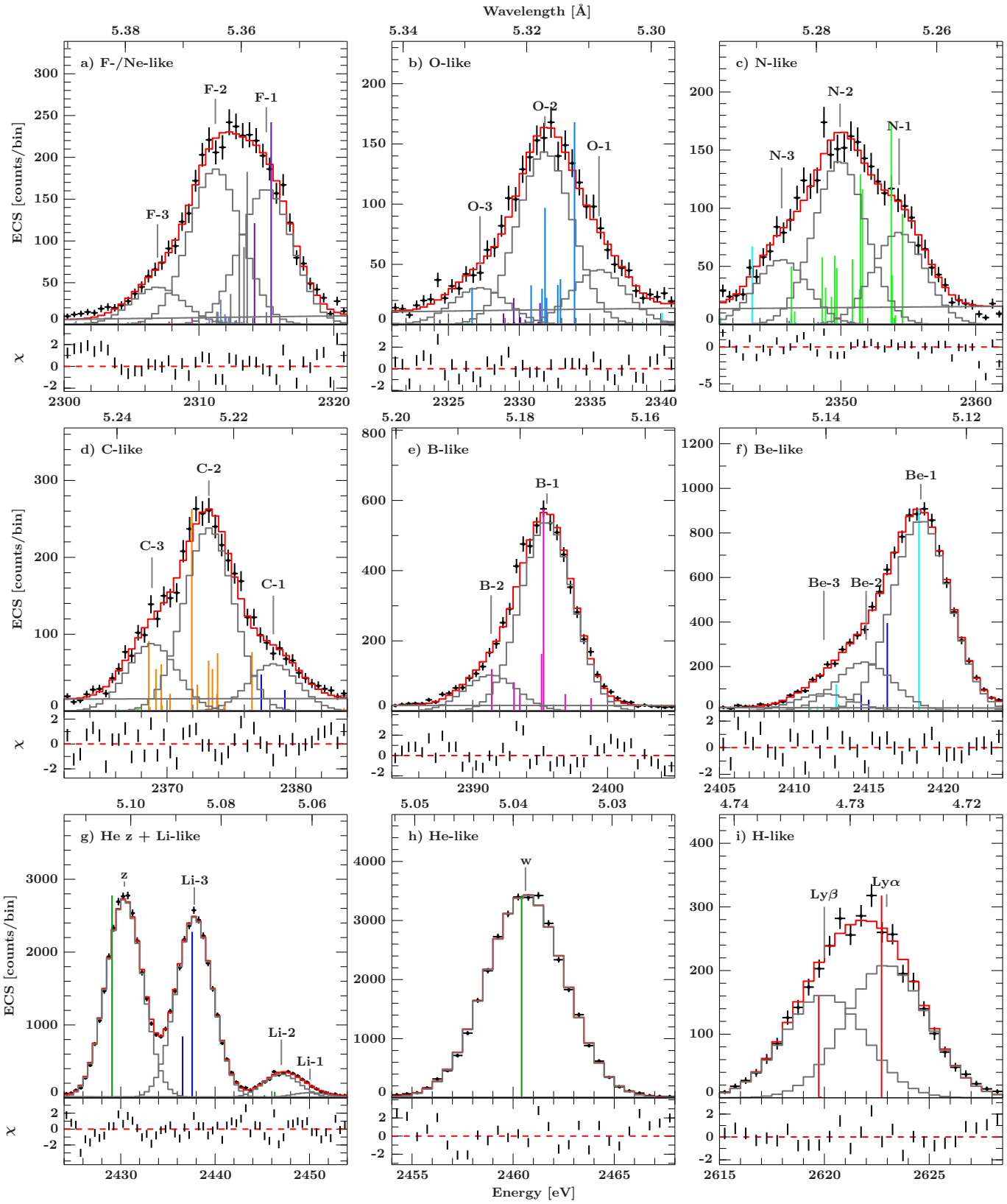

Figure A2. Same as Figure A1 for the S spectrum. Line labels denote transitions listed in Table A2.